arXiv:1405.3301v3 [nucl-ex] 16 Mar 2015

Heavy-quark production and elliptic flow in Au+Au collisions at $\sqrt{s_{NN}} = 62.4$ GeV

A. Adare,[12] C. Aidala,[36,41] N.N. Ajitanand,[58] Y. Akiba,[52,53] R. Akimoto,[11] H. Al-Ta'ani,[47] J. Alexander,[58] A. Angerami,[13] K. Aoki,[52] N. Apadula,[59] Y. Aramaki,[11,52] H. Asano,[32,52] E.C. Aschenauer,[7] E.T. Atomssa,[59] T.C. Awes,[49] B. Azmoun,[7] V. Babintsev,[23] M. Bai,[6] B. Bannier,[59] K.N. Barish,[8] B. Bassalleck,[46] S. Bathe,[5,53] V. Baublis,[51] S. Baumgart,[52] A. Bazilevsky,[7] R. Belmont,[63] A. Berdnikov,[55] Y. Berdnikov,[55] X. Bing,[48] D.S. Blau,[31] J.S. Bok,[47] K. Boyle,[53] M.L. Brooks,[36] H. Buesching,[7] V. Bumazhnov,[23] S. Butsyk,[46] S. Campbell,[59] P. Castera,[59] C.-H. Chen,[59] C.Y. Chi,[13] M. Chiu,[7] I.J. Choi,[24] J.B. Choi,[10] S. Choi,[57] R.K. Choudhury,[4] P. Christiansen,[38] T. Chujo,[62] O. Chvala,[8] V. Cianciolo,[49] Z. Citron,[59] B.A. Cole,[13] M. Connors,[59] M. Csanád,[17] T. Csörgő,[65] S. Dairaku,[32,52] A. Datta,[40] M.S. Daugherity,[1] G. David,[7] A. Denisov,[23] A. Deshpande,[53,59] E.J. Desmond,[7] K.V. Dharmawardane,[47] O. Dietzsch,[56] L. Ding,[27] A. Dion,[27,59] M. Donadelli,[56] O. Drapier,[33] A. Drees,[59] K.A. Drees,[6] J.M. Durham,[36,59] A. Durum,[23] L. D'Orazio,[39] S. Edwards,[6] Y.V. Efremenko,[49] T. Engelmore,[13] A. Enokizono,[49] S. Esumi,[62] K.O. Eyser,[8] B. Fadem,[42] D.E. Fields,[46] M. Finger,[9] M. Finger, Jr.,[9] F. Fleuret,[33] S.L. Fokin,[31] J.E. Frantz,[48] A. Franz,[7] A.D. Frawley,[19] Y. Fukao,[52] T. Fusayasu,[44] K. Gainey,[1] C. Gal,[59] A. Garishvili,[60] I. Garishvili,[35] A. Glenn,[35] X. Gong,[58] M. Gonin,[33] Y. Goto,[52,53] R. Granier de Cassagnac,[33] N. Grau,[2] S.V. Greene,[63] M. Grosse Perdekamp,[24] T. Gunji,[11] L. Guo,[36] H.-Å. Gustafsson,[38,*] T. Hachiya,[52] J.S. Haggerty,[7] K.I. Hahn,[18] H. Hamagaki,[11] J. Hanks,[13] K. Hashimoto,[52,54] E. Haslum,[38] R. Hayano,[11] X. He,[20] T.K. Hemmick,[59] T. Hester,[8] J.C. Hill,[27] R.S. Hollis,[8] K. Homma,[22] B. Hong,[30] T. Horaguchi,[62] Y. Hori,[11] S. Huang,[63] T. Ichihara,[52,53] H. Iinuma,[29] Y. Ikeda,[52,62] J. Imrek,[16] M. Inaba,[62] A. Iordanova,[8] D. Isenhower,[1] M. Issah,[63] D. Ivanishchev,[51] B.V. Jacak,[59] M. Javani,[20] J. Jia,[7,58] X. Jiang,[36] B.M. Johnson,[7] K.S. Joo,[43] D. Jouan,[50] D.S. Jumper,[24] J. Kamin,[59] S. Kaneti,[59] B.H. Kang,[21] J.H. Kang,[66] J.S. Kang,[21] J. Kapustinsky,[36] K. Karatsu,[32,52] M. Kasai,[52,54] D. Kawall,[40,53] A.V. Kazantsev,[31] T. Kempel,[27] A. Khanzadeev,[51] K.M. Kijima,[22] B.I. Kim,[30] C. Kim,[30] D.J. Kim,[28] E.-J. Kim,[10] H.J. Kim,[66] K.-B. Kim,[10] Y.-J. Kim,[24] Y.K. Kim,[21] E. Kinney,[12] Á. Kiss,[17] E. Kistenev,[7] J. Klatsky,[19] D. Kleinjan,[8] P. Kline,[59] Y. Komatsu,[11] B. Komkov,[51] J. Koster,[24] D. Kotchetkov,[48] D. Kotov,[51,55] A. Král,[14] F. Krizek,[28] G.J. Kunde,[36] K. Kurita,[52,54] M. Kurosawa,[52] Y. Kwon,[66] G.S. Kyle,[47] R. Lacey,[58] Y.S. Lai,[13] J.G. Lajoie,[27] A. Lebedev,[27] B. Lee,[21] D.M. Lee,[36] J. Lee,[18] K.B. Lee,[30] K.S. Lee,[30] S.H. Lee,[59] S.R. Lee,[10] M.J. Leitch,[36] M.A.L. Leite,[56] M. Leitgab,[24] B. Lewis,[59] S.H. Lim,[66] L.A. Linden Levy,[12] M.X. Liu,[36] B. Love,[63] C.F. Maguire,[63] Y.I. Makdisi,[6] M. Makek,[64,67] A. Manion,[59] V.I. Manko,[31] E. Mannel,[13] S. Masumoto,[11] M. McCumber,[12] P.L. McGaughey,[36] D. McGlinchey,[12,19] C. McKinney,[24] M. Mendoza,[8] B. Meredith,[24] Y. Miake,[62] T. Mibe,[29] A.C. Mignerey,[39] A. Milov,[64] D.K. Mishra,[4] J.T. Mitchell,[7] Y. Miyachi,[52,61] S. Miyasaka,[52,61] A.K. Mohanty,[4] H.J. Moon,[43] D.P. Morrison,[7,†] S. Motschwiller,[42] T.V. Moukhanova,[31] T. Murakami,[32,52] J. Murata,[52,54] T. Nagae,[32] S. Nagamiya,[29,52] J.L. Nagle,[12,‡] M.I. Nagy,[65] I. Nakagawa,[52,53] Y. Nakamiya,[22] K.R. Nakamura,[32,52] T. Nakamura,[52] K. Nakano,[52,61] C. Nattrass,[60] A. Nederlof,[42] M. Nihashi,[22,52] R. Nouicer,[7,53] N. Novitzky,[28] A.S. Nyanin,[31] E. O'Brien,[7] C.A. Ogilvie,[27] K. Okada,[53] A. Oskarsson,[38] M. Ouchida,[22,52] K. Ozawa,[11] R. Pak,[7] V. Pantuev,[25] V. Papavassiliou,[47] B.H. Park,[21] I.H. Park,[18] S.K. Park,[30] S.F. Pate,[47] L. Patel,[20] H. Pei,[27] J.-C. Peng,[24] H. Pereira,[15] D.Yu. Peressounko,[31] R. Petti,[7,59] C. Pinkenburg,[7] R.P. Pisani,[7] M. Proissl,[59] M.L. Purschke,[7] H. Qu,[1] J. Rak,[28] I. Ravinovich,[64] K.F. Read,[49,60] D. Reynolds,[58] V. Riabov,[51] Y. Riabov,[51] E. Richardson,[39] N. Riveli,[48] D. Roach,[63] G. Roche,[37,*] S.D. Rolnick,[8] M. Rosati,[27] B. Sahlmueller,[59] N. Saito,[29] T. Sakaguchi,[7] V. Samsonov,[45,51] M. Sano,[62] M. Sarsour,[20] S. Sawada,[29] K. Sedgwick,[8] R. Seidl,[52,53] A. Sen,[20] R. Seto,[8] D. Sharma,[64] I. Shein,[23] T.-A. Shibata,[52,61] K. Shigaki,[22] M. Shimomura,[62] K. Shoji,[32,52] P. Shukla,[4] A. Sickles,[7] C.L. Silva,[27] D. Silvermyr,[49] K.S. Sim,[30] B.K. Singh,[3] C.P. Singh,[3] V. Singh,[3] M. Slunečka,[9] R.A. Soltz,[35] W.E. Sondheim,[36] S.P. Sorensen,[60] M. Soumya,[58] I.V. Sourikova,[7] P.W. Stankus,[49] E. Stenlund,[38] M. Stepanov,[40] A. Ster,[65] S.P. Stoll,[7] T. Sugitate,[22] A. Sukhanov,[7] J. Sun,[59] J. Sziklai,[65] E.M. Takagui,[56] A. Takahara,[11] A. Taketani,[52,53] Y. Tanaka,[44] S. Taneja,[59] K. Tanida,[53,57] M.J. Tannenbaum,[7] S. Tarafdar,[3] A. Taranenko,[45,58] E. Tennant,[47] H. Themann,[59] T. Todoroki,[52,62] L. Tomášek,[26] M. Tomášek,[14,26] H. Torii,[22] R.S. Towell,[1] I. Tserruya,[64] Y. Tsuchimoto,[11] T. Tsuji,[11] C. Vale,[7] H.W. van Hecke,[36] M. Vargyas,[17] E. Vazquez-Zambrano,[13] A. Veicht,[13] J. Velkovska,[63] R. Vértesi,[65] M. Virius,[14] A. Vossen,[24] V. Vrba,[14,26] E. Vznuzdaev,[51] X.R. Wang,[47] D. Watanabe,[22] K. Watanabe,[62] Y. Watanabe,[52,53] Y.S. Watanabe,[11] F. Wei,[27] R. Wei,[58] S. Whitaker,[27] S.N. White,[7] D. Winter,[13] S. Wolin,[24] C.L. Woody,[7] M. Wysocki,[12] Y.L. Yamaguchi,[11,52] R. Yang,[24] A. Yanovich,[23] J. Ying,[20] S. Yokkaichi,[52,53] Z. You,[36] I. Younus,[34,46] I.E. Yushmanov,[31] W.A. Zajc,[13] and A. Zelenski[6]

(PHENIX Collaboration)

[1] *Abilene Christian University, Abilene, Texas 79699, USA*

[2]*Department of Physics, Augustana College, Sioux Falls, South Dakota 57197, USA*
[3]*Department of Physics, Banaras Hindu University, Varanasi 221005, India*
[4]*Bhabha Atomic Research Centre, Bombay 400 085, India*
[5]*Baruch College, City University of New York, New York, New York, 10010 USA*
[6]*Collider-Accelerator Department, Brookhaven National Laboratory, Upton, New York 11973-5000, USA*
[7]*Physics Department, Brookhaven National Laboratory, Upton, New York 11973-5000, USA*
[8]*University of California - Riverside, Riverside, California 92521, USA*
[9]*Charles University, Ovocný trh 5, Praha 1, 116 36, Prague, Czech Republic*
[10]*Chonbuk National University, Jeonju, 561-756, Korea*
[11]*Center for Nuclear Study, Graduate School of Science, University of Tokyo, 7-3-1 Hongo, Bunkyo, Tokyo 113-0033, Japan*
[12]*University of Colorado, Boulder, Colorado 80309, USA*
[13]*Columbia University, New York, New York 10027 and Nevis Laboratories, Irvington, New York 10533, USA*
[14]*Czech Technical University, Zikova 4, 166 36 Prague 6, Czech Republic*
[15]*Dapnia, CEA Saclay, F-91191, Gif-sur-Yvette, France*
[16]*Debrecen University, H-4010 Debrecen, Egyetem tér 1, Hungary*
[17]*ELTE, Eötvös Loránd University, H - 1117 Budapest, Pázmány P. s. 1/A, Hungary*
[18]*Ewha Womans University, Seoul 120-750, Korea*
[19]*Florida State University, Tallahassee, Florida 32306, USA*
[20]*Georgia State University, Atlanta, Georgia 30303, USA*
[21]*Hanyang University, Seoul 133-792, Korea*
[22]*Hiroshima University, Kagamiyama, Higashi-Hiroshima 739-8526, Japan*
[23]*IHEP Protvino, State Research Center of Russian Federation, Institute for High Energy Physics, Protvino, 142281, Russia*
[24]*University of Illinois at Urbana-Champaign, Urbana, Illinois 61801, USA*
[25]*Institute for Nuclear Research of the Russian Academy of Sciences, prospekt 60-letiya Oktyabrya 7a, Moscow 117312, Russia*
[26]*Institute of Physics, Academy of Sciences of the Czech Republic, Na Slovance 2, 182 21 Prague 8, Czech Republic*
[27]*Iowa State University, Ames, Iowa 50011, USA*
[28]*Helsinki Institute of Physics and University of Jyväskylä, P.O.Box 35, FI-40014 Jyväskylä, Finland*
[29]*KEK, High Energy Accelerator Research Organization, Tsukuba, Ibaraki 305-0801, Japan*
[30]*Korea University, Seoul, 136-701, Korea*
[31]*Russian Research Center "Kurchatov Institute", Moscow, 123098 Russia*
[32]*Kyoto University, Kyoto 606-8502, Japan*
[33]*Laboratoire Leprince-Ringuet, Ecole Polytechnique, CNRS-IN2P3, Route de Saclay, F-91128, Palaiseau, France*
[34]*Physics Department, Lahore University of Management Sciences, Lahore, Pakistan*
[35]*Lawrence Livermore National Laboratory, Livermore, California 94550, USA*
[36]*Los Alamos National Laboratory, Los Alamos, New Mexico 87545, USA*
[37]*LPC, Université Blaise Pascal, CNRS-IN2P3, Clermont-Fd, 63177 Aubiere Cedex, France*
[38]*Department of Physics, Lund University, Box 118, SE-221 00 Lund, Sweden*
[39]*University of Maryland, College Park, Maryland 20742, USA*
[40]*Department of Physics, University of Massachusetts, Amherst, Massachusetts 01003-9337, USA*
[41]*Department of Physics, University of Michigan, Ann Arbor, Michigan 48109-1040, USA*
[42]*Muhlenberg College, Allentown, Pennsylvania 18104-5586, USA*
[43]*Myongji University, Yongin, Kyonggido 449-728, Korea*
[44]*Nagasaki Institute of Applied Science, Nagasaki-shi, Nagasaki 851-0193, Japan*
[45]*National Research Nuclear University, MEPhI, Moscow Engineering Physics Institute, Moscow, 115409, Russia*
[46]*University of New Mexico, Albuquerque, New Mexico 87131, USA*
[47]*New Mexico State University, Las Cruces, New Mexico 88003, USA*
[48]*Department of Physics and Astronomy, Ohio University, Athens, Ohio 45701, USA*
[49]*Oak Ridge National Laboratory, Oak Ridge, Tennessee 37831, USA*
[50]*IPN-Orsay, Universite Paris Sud, CNRS-IN2P3, BP1, F-91406, Orsay, France*
[51]*PNPI, Petersburg Nuclear Physics Institute, Gatchina, Leningrad region, 188300, Russia*
[52]*RIKEN Nishina Center for Accelerator-Based Science, Wako, Saitama 351-0198, Japan*
[53]*RIKEN BNL Research Center, Brookhaven National Laboratory, Upton, New York 11973-5000, USA*
[54]*Physics Department, Rikkyo University, 3-34-1 Nishi-Ikebukuro, Toshima, Tokyo 171-8501, Japan*
[55]*Saint Petersburg State Polytechnic University, St. Petersburg, 195251 Russia*
[56]*Universidade de São Paulo, Instituto de Física, Caixa Postal 66318, São Paulo CEP05315-970, Brazil*
[57]*Department of Physics and Astronomy, Seoul National University, Seoul, Korea*
[58]*Chemistry Department, Stony Brook University, SUNY, Stony Brook, New York 11794-3400, USA*
[59]*Department of Physics and Astronomy, Stony Brook University, SUNY, Stony Brook, New York 11794-3800,, USA*
[60]*University of Tennessee, Knoxville, Tennessee 37996, USA*
[61]*Department of Physics, Tokyo Institute of Technology, Oh-okayama, Meguro, Tokyo 152-8551, Japan*
[62]*Institute of Physics, University of Tsukuba, Tsukuba, Ibaraki 305, Japan*
[63]*Vanderbilt University, Nashville, Tennessee 37235, USA*
[64]*Weizmann Institute, Rehovot 76100, Israel*

[65] Institute for Particle and Nuclear Physics, Wigner Research Centre for Physics, Hungarian Academy of Sciences (Wigner RCP, RMKI) H-1525 Budapest 114, POBox 49, Budapest, Hungary
[66] Yonsei University, IPAP, Seoul 120-749, Korea
[67] University of Zagreb, Faculty of Science, Department of Physics, Bijenička 32, HR-10002 Zagreb, Croatia
(Dated: March 17, 2015)

We present measurements of electrons and positrons from the semileptonic decays of heavy-flavor hadrons at midrapidity ($|y| < 0.35$) in Au+Au collisions at $\sqrt{s_{NN}} = 62.4$ GeV. The data were collected in 2010 by the PHENIX experiment that included the new hadron-blind detector. The invariant yield of electrons from heavy-flavor decays is measured as a function of transverse momentum in the range $1 < p_T^e < 5$ GeV/c. The invariant yield per binary collision is slightly enhanced above the p+p reference in Au+Au 0%–20%, 20%–40% and 40%–60% centralities at a comparable level. At this low beam energy this may be a result of the interplay between initial-state Cronin effects, final-state flow, and energy loss in medium. The v_2 of electrons from heavy-flavor decays is nonzero when averaged between $1.3 < p_T^e < 2.5$ GeV/c for 0%–40% centrality collisions at $\sqrt{s_{NN}} = 62.4$ GeV. For 20%–40% centrality collisions, the v_2 at $\sqrt{s_{NN}} = 62.4$ GeV is smaller than that for heavy flavor decays at $\sqrt{s_{NN}} = 200$ GeV. The v_2 of the electrons from heavy-flavor decay at the lower beam energy is also smaller than v_2 for pions. Both results indicate that the heavy-quarks interact with the medium formed in these collisions, but they may not be at the same level of thermalization with the medium as observed at $\sqrt{s_{NN}} = 200$ GeV.

PACS numbers: 25.75.Dw

I. INTRODUCTION

Collisions of large nuclei at ultra-relativistic energies produce a state of matter, known as the quark-gluon plasma (QGP), in which the quarks and gluons that are normally bound inside hadrons become deconfined. At the Relativistic Heavy Ion Collider (RHIC), collisions of heavy nuclei at $\sqrt{s_{NN}} = 200$ GeV produce strongly coupled, dense partonic matter that exhibits strong collective motion [1]. Comparisons of the measured anisotropic flow parameter v_2 with hydrodynamic calculations indicate that the medium expands and flows as a near-perfect liquid [2–4]. The significant suppression of high-p_T particles produced in these collisions relative to scaled p+p collisions at the same center of mass energy also implies that partons lose energy while traversing the medium [5–7]. Both results indicate the formation of the QGP at $\sqrt{s_{NN}} = 200$ GeV. It is important to map out these two key observations as a function of collision energy to study the transition from normal hadronic matter to the QGP.

Due to the short lifetime of the hot nuclear medium (~ 10 fm/c), experimental probes of the medium properties must be self-generated during the collision. To explore the formation and properties of strongly interacting matter at lower energy density, a particularly useful set of probes is charm and bottom quarks. At RHIC energies these quarks are produced primarily through gluon fusion in the initial stage of the collision, and are therefore present for the full evolution of the system, in contrast to the lighter quarks that can be produced thermally throughout the lifetime of the medium. Prior experiments have established that electrons from heavy flavor meson decays display a significant v_2 in Au+Au collisions at $\sqrt{s_{NN}} = 200$ GeV and Pb+Pb collisions at $\sqrt{s_{NN}} = 2.76$ TeV, indicating that heavy quarks may experience collective motion along with the lighter partons that constitute the bulk of the medium [8–10]. In contrast with early predictions [11, 12], heavy flavor hadrons are also significantly suppressed in central Au+Au collisions at $\sqrt{s_{NN}} = 200$ GeV, at a level comparable to light-flavor hadrons [8, 9]. The magnitude of the suppression and flow of heavy quarks have proven to be a challenge to many models of parton energy loss in QGP [13–16].

To explore the formation and properties of lower energy density strongly interacting matter, Au+Au collisions with lower center of mass energies (62.4, 39, 11.5. and 7.7 GeV) were recorded during the 2010 RHIC run. It was observed that inclusive hadrons and identified light-flavor hadrons display significant flow in Au+Au collisions at $\sqrt{s_{NN}} = 62.4$ GeV [17, 18]. However, the observed π^0 suppression is smaller than in higher energy collisions [19] for $p_T < 6$ GeV/c. This may be due to a change in the competition between the Cronin enhancement that is prevalent in lower energy collisions and the suppressing effects of the hot medium [20]. Cronin enhancement is also observed for electrons from heavy-flavor decays in d+Au collisions at $\sqrt{s_{NN}} = 200$ GeV [21], and is expected to be larger at lower energies [22].

To provide more information on the formation and properties of the plasma produced at $\sqrt{s_{NN}} = 62.4$ GeV at RHIC, and the possible role of initial-state effects, this paper presents measurements of the p_T spectra and anisotropic flow parameter v_2 of electrons from the decays of heavy flavor (charm and beauty) hadrons produced in Au+Au collisions.

* Deceased
† PHENIX Co-Spokesperson: morrison@bnl.gov
‡ PHENIX Co-Spokesperson: jamie.nagle@colorado.edu

II. EXPERIMENT SETUP

PHENIX collected approximately 400 million events in 2010 for Au+Au collisions at $\sqrt{s_{NN}} = 62.4$ GeV within ± 20 cm of the nominal collision point. Figure 1 shows the PHENIX detector system during the 2010 data taking period. Details about PHENIX detector subsystems can be found in Refs. [23–31].

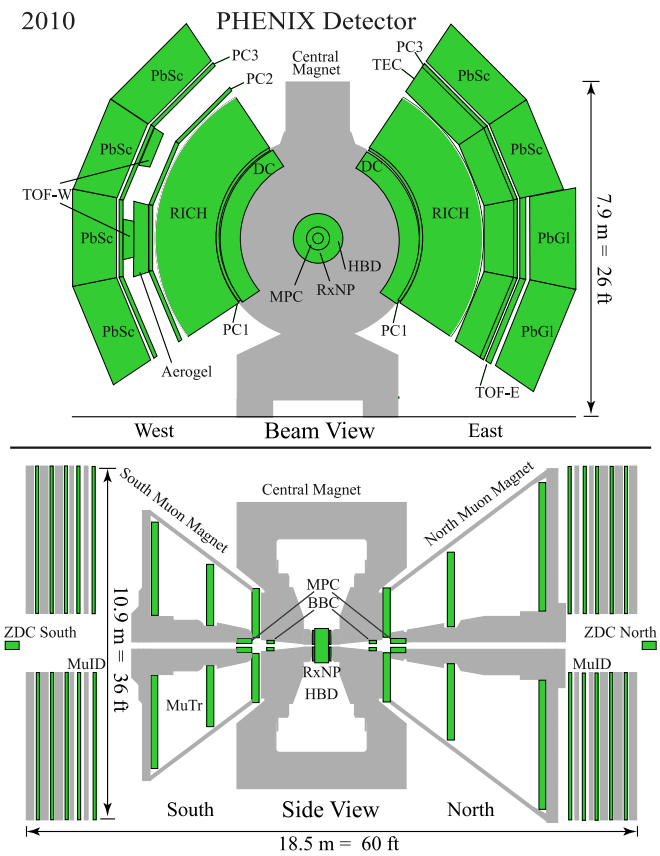

FIG. 1. (Color online) The PHENIX detector configuration for the 2010 data taking period. The upper panel is the beam view and the lower panel is the side view.

The beam-beam counters (BBC) provide the measurement of collision time, collision vertex position along the beam axis, and the minimum-bias (MB) trigger information [24]. BBCs are installed along the beam axis 144 cm from the center of PHENIX with a rapidity coverage of $3.0 < |\eta| < 3.9$. The difference of the average hit time of PMTs between the North and the South BBC determines the collision vertex position along the beam direction, producing a vertex resolution in the beam direction of $\sim$0.5 cm in central Au+Au collisions. The event centrality is also determined by the BBC. For the purpose of this analysis, the total charge in the BBC is divided into four centrality categories: 0%–20%, 20%–40%, 40%–60%, and 60%–86%. The statistical significance of the data in the most peripheral bin (60%–86%) was too low to provide a useful measurement. The MB trigger efficiency is $85.9 \pm 2.0\%$ of the total Au+Au inelastic cross section at $\sqrt{s_{NN}} = 62.4$ GeV. All MB data presented are calculated directly from the MB event sample.

The reaction-plane detector (RXNP) is a plastic scintillator paddle detector installed prior to the 2007 data-taking period [25]. It accurately measures the participant reaction-plane (RP) angle defined by the beam axis and the principal axis of the participant zone. The RXNP is located at $\pm$ 39 cm along the beam pipe from the center of PHENIX with a set of 24 scintillators in each arm.

In this paper, heavy-flavor hadrons are measured indirectly through electrons from the semi-leptonic decay channel. The two PHENIX central arm spectrometers (CA), which cover $|\eta| < 0.35$ and $|\Delta\phi| = \pi/2$ each, provide track reconstruction, momentum and energy measurement, and electron identification (eID) for this analysis. Based on the electron's bend in the magnetic field, the drift chambers and pad chambers reconstruct the track momentum with high resolution. The size and shape of the Čerenkov ring detected in the ring imaging Čerenkov detector (RICH) is used for electron identification over the full momentum range. Pions that fire the RICH above 5 GeV/c are statistically insignificant. In addition, the electromagnetic calorimeter (EMCal) measures the energy deposited by electrons and their shower shape. The energy-to-momentum ratio and the quality of matching of the shower shape to a particle template are used for eID in a manner similar to the method used in [9].

In the 2010 run the hadron-blind detector (HBD) was also installed in PHENIX [27]. The HBD is a windowless Čerenkov detector that uses CF_4 gas as the radiator and amplification gas, in a container with a radius of $\approx$60 cm. The radiator is directly coupled in a windowless configuration to a readout element with a triple gas-electron-multiplier (GEM) stack. The HBD is almost completely insensitive to hadrons up to around 4.5 GeV/c when operated with a reverse-bias voltage, and therefore brings additional eID capability. The HBD can also reduce background electrons from π^0 Dalitz decays and photon conversions in the detector material, especially conversions in the beampipe and entrance window into the HBD. A nearly field-free region in the HBD area (currents in the inner and outer coils of the central arm spectrometer magnets flow in opposite directions) preserves the opening angle of electron pairs and, given the large size of the readout pads, signals from a close pair will overlap on a cluster of neighboring pads. The π^0 Dalitz and conversion e^+e^- pairs have small opening angles, and can therefore be rejected, while single electrons or electron pairs with large opening angles leave a signal of $\sim$ 20 photoelectrons (p.e.) in the HBD.

III. DATA ANALYSIS

A. Candidate Electron Measurement

To select data recorded with the optimum detector response, we use the average number of electrons and positrons per event in each run and reject those runs where the electron multiplicity deviates from the mean multiplicity by more than 3σ. To select good quality tracks, we follow the same method as described in [9]. The minimum transverse momentum for charged tracks in this analysis p_T is greater than 1.0 GeV/c. For a track to be identified as an electron candidate, it is also required to fire the RICH and EMCal detectors, and to be associated with at least 4 fired phototubes in the RICH ring. In addition, the E/p distribution, where E is the energy deposited in the EMCal and p is the momentum of the track reconstructed by the drift chambers, is used to select electron candidates. Electrons deposit most of their energy in the EMCal which makes E/p close to 1, while hadrons deposit only part of the energy in EMCal which causes E/p to be smaller. A cut of $dep > -2$ was used, where $dep = \frac{E/p-1}{\sigma_{E/p}}$.

In addition to the above electron cuts, the HBD provides electron identification and background rejection. We apply cuts on *hbdq*, where *hbdq* is the number of p.e. recorded by the HBD in a cluster. Most of the hadrons and back plane conversion electrons are not associated with an HBD cluster; the rest can be divided into three categories:

1. The track is a single electron (our signal) or an electron or positron from an electron pair with large opening angle; either case will produce an *hbdq* distribution centered at 20 p.e.

2. The cluster comes from an electron pair with small opening angle which will produce an *hbdq* distribution centered at 40 p.e.

3. The track does not fire the HBD itself, but is randomly associated with a fake cluster that is formed from the fluctuating HBD background. Charged particles traversing the CF_4 volume in the HBD produce scintillation light and creates hits with a small signal in random locations. In this case the *hbdq* distribution has low values with an exponential shape. The minimum *hbdq* cut removes most of these HBD background hits. A portion of these fluctuate to a larger *hbdq* signal, but are statistically subtracted as described later in this section.

A cut of $10 < hbdq < 35$ reduces the backgrounds due to cases 2 and 3. A swapping method is used to statistically remove the background from case 3, i.e. random track associations with HBD background, including conversions that are randomly associated with HBD clusters. The swapped HBD charge ($hbdq_s$) is obtained by matching in software a track found in the central arm to the HBD in the opposite arm, for example from HBD hits in the east arm to tracks in the west arm and vice versa. The swapped *hbdq* distribution was normalized to the *hbdq* in the bins near zero charge. Figure 2 shows the regular *hbdq* distribution, the swapped $hbdq_s$ and the distribution after subtraction.

The swapped distribution, representing the *hbdq* distribution for randomly associated tracks, falls rapidly. The swapped random coincidences produce signals at low E/p as well as a peak centered at E/p near 1. The low E/p distribution is most probably random hadron coincidences and the peak is likely dominated by conversion electrons from the back plane of the HBD having a random coincidence with background clusters in the HBD. After subtracting the swapped distribution from the regular distribution, the *hbdq* distribution has a peak around 20 p.e. and a long tail at high charge that is a superposition of the distribution of the single electron signal and the distribution of the close pair signal. To establish the extent of the remaining hadron contamination, the *dep* distribution after subtraction is fit with a falling exponential (hadrons) and a Gaussian peaked close to 1 (electrons). The contamination changes with p_T and centrality; it is largest at low p_T and more central collisions. At p_T near 1 GeV/c, the contamination is 2% in the peripheral bin of 40%–60%, 4% in 20%–40% centrality collisions, and 8% in 0%–20% central collisions. For $p_T > 2$ GeV/c, the contamination is approximately independent of p_T at 2%, 2.5%, and 3% for the centrality bins 40%–60%, 20%–40% and 0%–20% respectively. The yield within the range $10 < hbdq < 35$ of the swapped HBD charge distribution is subtracted at each p_T.

This swapping technique is repeated for each centrality and all distributions after subtraction are shown in Fig. 2. In addition, the *hbdq* distributions (subtracted or unsubtracted) broaden because of increasing fluctuations of the scintillation background in more central events. This will change the efficiency of the *hbdq* cut as described in the subsection III B.

The distributions after subtraction are shown in Fig. 3 for different p_T. The shape of the subtracted *hbdq* distribution does not vary noticeably between 0.75 and 2.5 GeV/c. In central collisions, applying the $10 < hbdq < 35$ cut rejects 38% of the tracks that satisfied the central arm's eID selection. This fraction is 35% for peripheral collisions. Some conversions still remain after the *hbdq* cut and the swapping subtraction: these are subtracted using a simulated cocktail. The cocktail simulations are described in the subsection III D.

B. Simulations

We use a GEANT [32] simulation to estimate the efficiency loss because of the inactive areas and the eID cuts. This simulation has been demonstrated to match the central-arm PID and tracking-chamber performance as described in [9] and is used to determine the single-

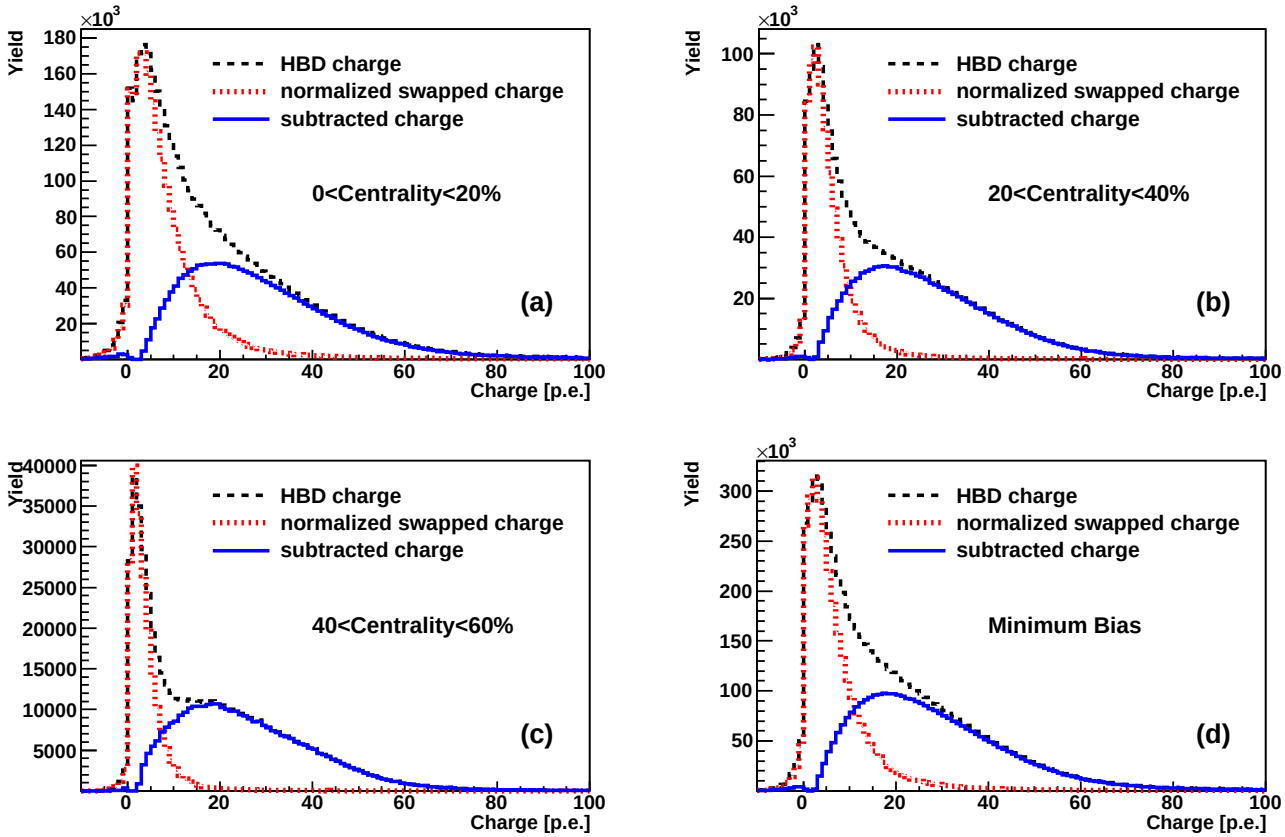

FIG. 2. (Color online) For centralities (a) 0%–20% (most central), (b) 20%–40%, (c) 40%–60%, and (d) MB events, shown are the shapes of the HBD charge distribution (black dashed curves), the swapped HBD charge distribution (red dotted curves), and the subtracted HBD charge distribution (blue solid curves). The swapped HBD distribution can statistically estimate the randomly matched HBD charges.

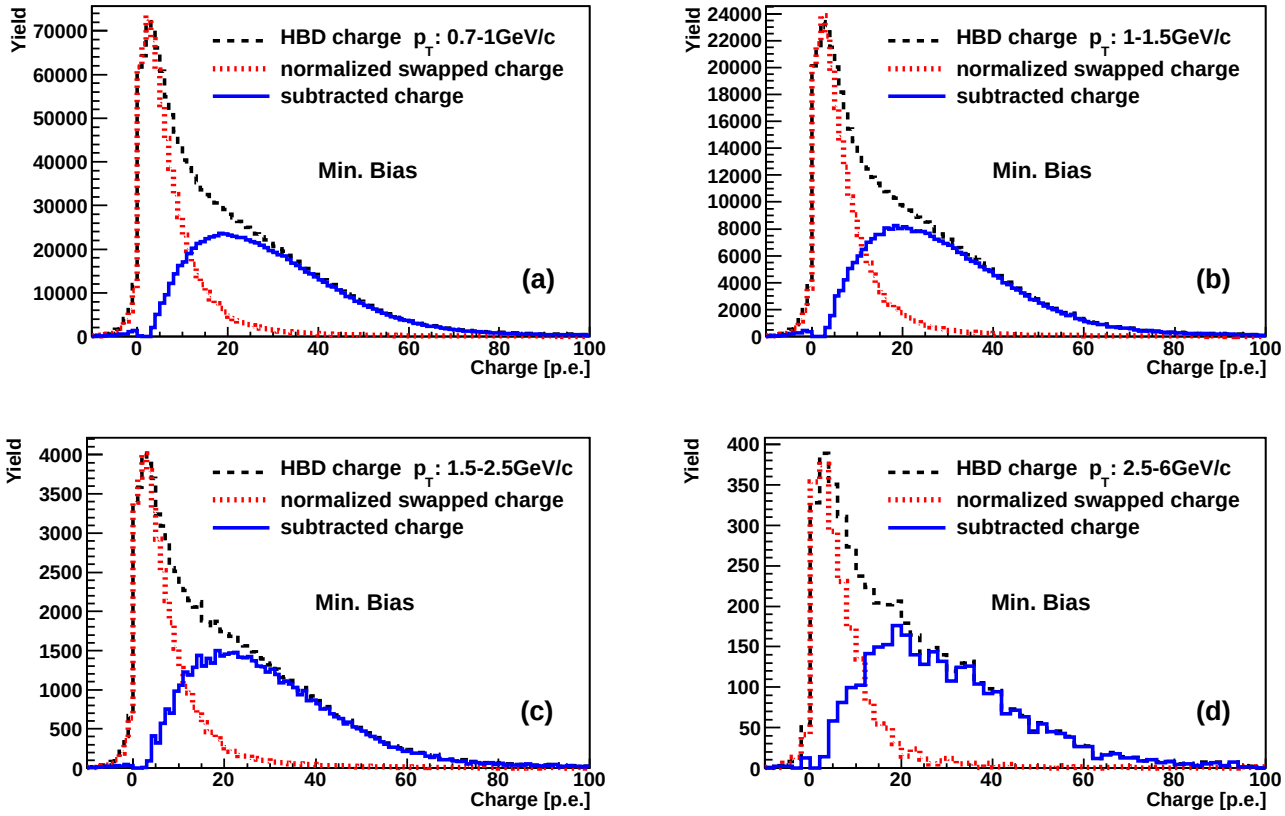

FIG. 3. (Color online) The shape of the HBD charge distribution (black dashed curves), the swapped HBD charge distribution (red dotted curves) and the subtracted HBD charge distribution (blue solid curve) for the indicated p_T ranges. All plots are

electron central-arm acceptance and efficiency. Because single electrons and close electron pairs have different *hbdq* distributions, the efficiency of the HBD cut is different for electrons from different sources. Hence we use a cocktail of a variety of sources, the relative importance of which is constrained by available measured yields of different mesons. Figure 4 shows how well the HBD charge response is described by the HBD simulation. The simulation has a bump at $hbdq \sim 45$, which is not observed in the data.

The HBD efficiency is 75% for the single electrons in the simulation (and for electrons from pairs with very large opening angles). Within the simulation, we can examine which electron pairs are removed by the *hbdq* cut. This rejects 65% of electrons that come from pairs that have a decay opening angle less than 0.05 radians while the rejection decreases until the opening angles reaches 0.1 radian. For each meson source in the cocktail, the efficiency is separately mapped as a function of p_T and is used to correct the data.

We embed the simulated HBD single track response into real events to evaluate the centrality dependence of the HBD efficiency. For single electrons, the simulated *hbdq* distribution is approximately Gaussian with a peak near 20. This broadens and shifts to a slightly higher average when embedded into a Au+Au event. The embedding efficiency for the fixed cut of $10 < hbdq < 35$ is calculated as a function of centrality and p_T. To understand the dependence of the efficiency on these two variables, we integrate over each in turn. Figure 5(b) shows the p_T dependence integrated over centrality, which is approximately 75% efficient independent of p_T. This lack of p_T dependence of the HBD cut efficiency is also observed in other centrality classes, but as seen in Fig. 5(a) the average efficiency does decrease for more central collisions; for central Au+Au events the efficiency has decreased to 65%. As discussed earlier this is because of increased fluctuation of the underlying event background, mostly because of scintillation in the CF_4 gas.

The acceptance and efficiency corrections are applied to the raw yields to produce the invariant yield of the electron candidates measured in Au+Au collisions at $\sqrt{s_{NN}} = 62.4$ GeV for different centrality bins as shown in Fig. 6, where

$$E\frac{d^3N}{d^3p} = \frac{1}{2\pi p_T}\frac{1}{dydp_T}\frac{1}{A\times\epsilon\times\epsilon_{\rm HBD}}\frac{N(e^+ + e^-)}{2}\frac{1}{N_{\rm events}}, \quad (1)$$

where $N(e^+ + e^-)$ is the number of electrons and positrons after HBD cuts, and after both swapped coincidences and hadron background contamination have been subtracted; $A\times\epsilon$ is the acceptance and efficiency of the central arm with eID cuts, including embedding efficiency; and $\epsilon_{\rm HBD}$ is the efficiency of HBD cuts including embedding. In subsection III D a cocktail is used to subtract the remaining background statistically.

TABLE I. $N_{\rm coll}$ values and RP resolution for each centrality class.

centrality class	$N_{\rm coll}$	RP resolution
0%–20%	689.9± 78.9	0.53
20%–40%	270.5± 27.5	0.62
40%–60%	85.7± 9.1	0.42

C. Azimuthal anisotropy measurement of candidate electrons

For candidate electrons comprising photonic electrons and electrons from heavy flavor decay, we also measure the azimuthal anisotropy v_2, which is the second Fourier coefficient of the azimuthal distribution of the candidate electron yield with respect to the participant RP:

$$\frac{dN}{d\phi} = N_0(1 + 2v_2\cos 2(\phi - \Phi_{\rm RP})), \quad (2)$$

where ϕ is the azimuthal angle of the electron track, $\Phi_{\rm RP}$ is the azimuthal angle of the participant RP, and N_0 is a normalization constant.

The participant RP is the plane formed by the transverse principal axis of the participants and the beam direction. The RXNP detector is used to measure the participant RP event by event. The event plane is constructed in two different windows: the South or North side of the RXNP. From these two planes we can calculate (Eq. 3) the RP resolution.

$$\langle\cos(2[\Phi_{\rm meas} - \Phi_{\rm real}])\rangle = \sqrt{2\langle\cos(2[\Phi_m^S - \Phi_m^N])\rangle}, \quad (3)$$

where Φ_m^S, Φ_m^N is the measured RP using only South or North side of the detector. The RP resolution is listed in Table I along with the number of binary collisions, $N_{\rm coll}$, for each of the three centrality classes. $N_{\rm coll}$ was determined using a Glauber Monte Carlo calculation.

Figure 7 shows the candidate electron yield with respect to the participant RP ($\phi - \Phi_{\rm RP}$) for selected p_T range for the 20%–40% centrality bin. The distribution is fitted with Eq. 2 to extract ${v_2}^{\rm raw}$. By correcting the ${v_2}^{\rm raw}$ with the RP resolution (Eq. 4), v_2 of the particle distribution with respect to the real RP can be measured.

$$v_2 = \frac{v_2^{\rm raw}}{\langle\cos(2[\Phi_{\rm meas} - \Phi_{\rm real}])\rangle}, \quad (4)$$

where $\Phi_{\rm meas}$ and $\Phi_{\rm real}$ are the measured and real RP angle. After correction by the RP resolution with Eq. 4, the candidate electron v_2 for different centrality bins is shown in Fig. 8.

D. Cocktail Subtraction

As described above, the cut on *hbdq* and the swapped subtraction removes most, but not all, of the background

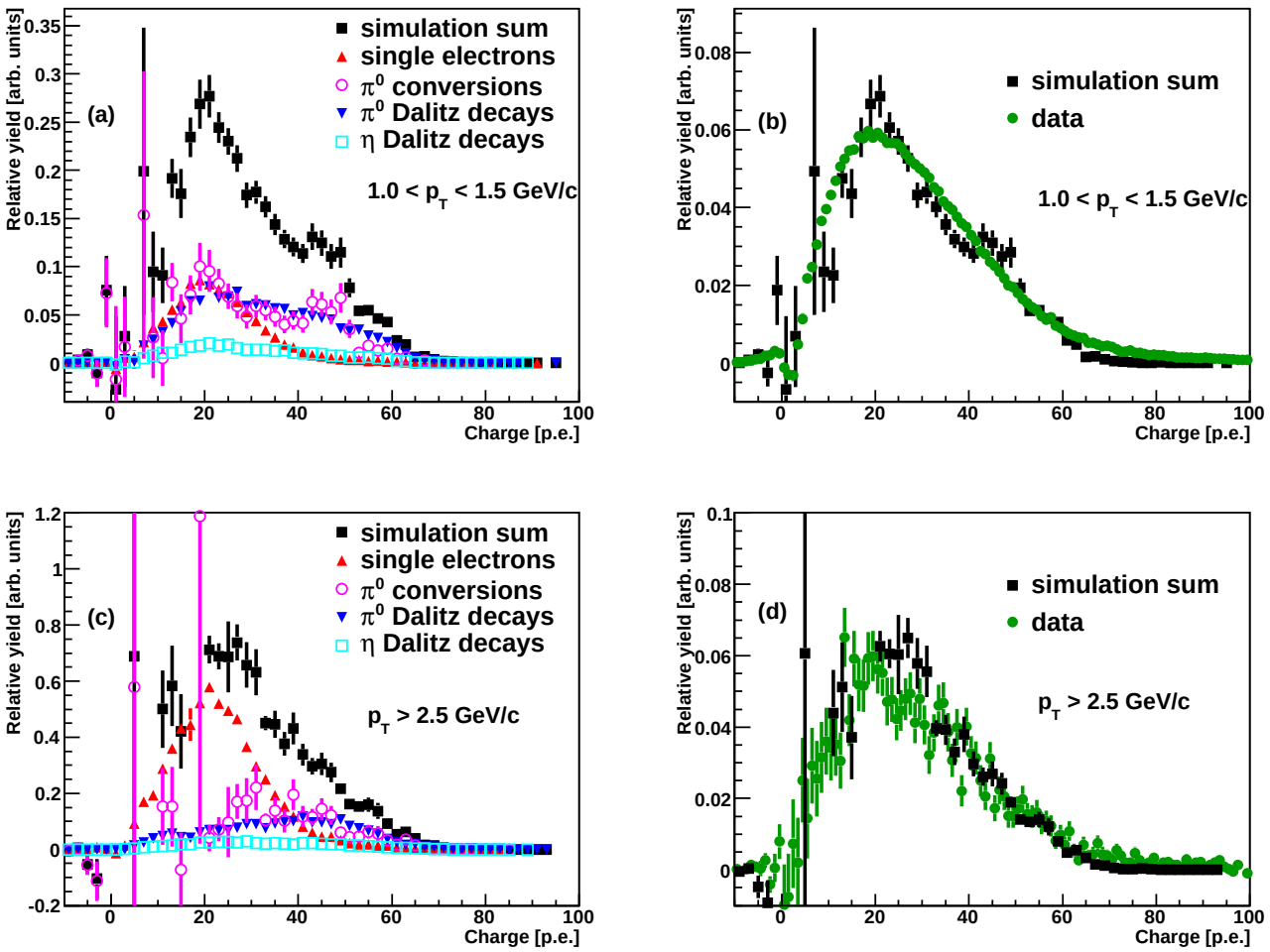

FIG. 4. (Color online) Simulated response of the HBD to different sources of electrons compared to the measured distribution for two different p_T ranges, (a) $1.0 < p_T < 1.5$ GeV/c and (c) $p_T > 2.5$ GeV/c. (black squares) total simulation, (red triangles) single electrons, (blue inverted triangles) π^0 Dalitz decays, (open magenta circles) conversions, (open cyan squares) η Dalitz decays, and (green circles) data. For visual comparison, in (b) and (d) the distributions are normalized to 1 for the same p_T ranges as in (a) and (c).

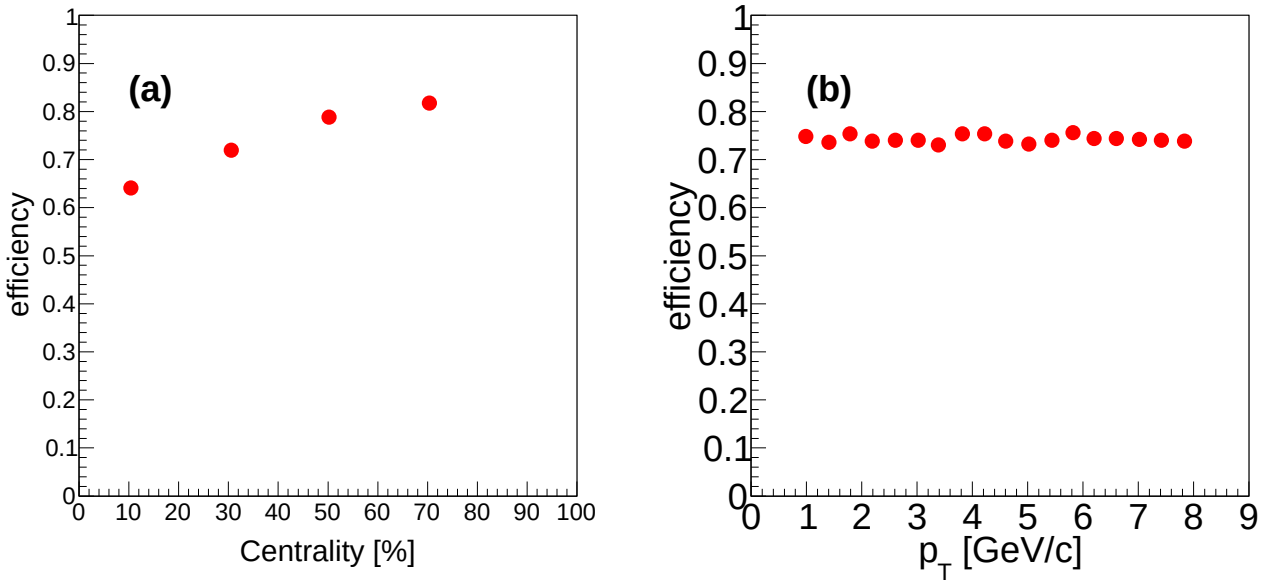

FIG. 5. (Color online) The efficiency of the HBD cut, $10 < hbdq < 35$, for a single electron as a function of (a) centrality and (b) p_T. The efficiency was determined by embedding a simulated single-electron response into the real data.

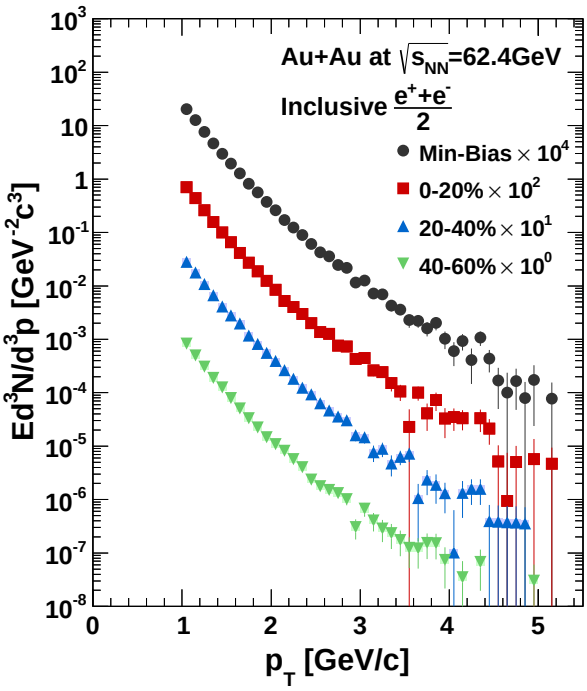

FIG. 6. (Color online) Invariant yield of candidate electrons measured in Au+Au collisions at $\sqrt{s_{NN}}$ =62.4 GeV for different centrality bins. The yields are scaled by powers of 10 for clarity. The systematic uncertainty is shown as boxes and is, in many cases, comparable to the symbol size.

from photonic decays. In this section we describe the cocktail method of statistically subtracting the remaining electrons. A Monte Carlo event generator is used to produce electrons from hadron decays; the cocktail includes the photonic sources listed below:

- Dalitz decays of neutral mesons: $X \longrightarrow \gamma + e^- + e^+$, where $X = \pi^0, \eta, \eta', \rho, \omega, \phi$
- Dilepton decays of neutral mesons: $X \longrightarrow e^- + e^+$, where $X = \rho, \omega, \phi$
- Conversions of decay photons (including Dalitz) in detector material
- K_{e3} decays ($K \longrightarrow \pi^{\mp} + e^{\pm} + \nu_e^{(-)}$)
- Conversion of direct photons

The cocktail yield (Y) is calculated as

$$\begin{aligned} Y = & \sum \epsilon_{\rm decay}({\rm hadron}, p_T) \times Y_{\rm decay}({\rm hadron}, p_T) \\ & + \sum \epsilon_{\rm conversion}(p_T) \times R_{\rm CD}(p_T) \times Y_{\rm Dalitz}({\rm hadron}, p_T) \\ & + \epsilon_{K_{e3}}(p_T) \times Y_{\rm decay}(K_{e3}, p_T) \\ & + \epsilon_{\rm conversion}(p_T) \times Y_{\rm Conversionofdirectphotons}(p_T) \end{aligned} \quad (5)$$

where $Y_{\rm decay}({\rm hadron}, p_T)$ is the yield of Dalitz and dilepton decays of neutral mesons. The efficiency and acceptance for each source are different as described in the subsection III B. For example, the efficiency for Dalitz decays of π^0 decreases from 0.5 at $p_T = 1$ GeV/c to 0.3 at $p_T = 5$ GeV/c. Heavier mesons have larger opening angles and hence a higher probability for satisfying the HBD cuts. For instance, η decays have an efficiency of 0.6 at $p_T = 1$ GeV/c and 0.45 at $p_T = 5$ GeV/c. The conversion electrons are proportional to Dalitz decays with a proportionality factor $R_{\rm CD}$ based on simulation. $R_{\rm CD}$ is 0.9 at $p_T = 1$ GeV/c and increases linearly to to 1.4 at $p_T = 5$ GeV/c. This cocktail is constrained by the measured π^0 p_T spectra in Au+Au collisions at $\sqrt{s_{NN}} = 62.4$ GeV [19] which is fit to Eq. 6 for each centrality.

$$E\frac{d^3N}{d^3p_T} = \frac{c}{(e^{-ap_T - bp_T^2} + \frac{p_T}{p_0})^n}, \quad (6)$$

where a, b, c, n and p_0 are fit parameters. The relative normalization of other mesons to π^0 can be obtained from the meson to pion ratios at high p_T [33–35]

- $\eta/\pi = 0.48 \pm 0.03$
- $\phi/\pi = 1.00 \pm 0.30$
- $\omega/\pi = 0.90 \pm 0.06$
- $\eta'/\pi = 0.25 \pm 0.075$
- $\eta/\pi = 0.40 \pm 0.12$

and the shapes of the spectra assuming m_T scaling, i.e. replace p_T with $m_T = \sqrt{{p_T}^2 + {m_{\rm meson}}^2 - {m_{\pi^0}}^2}$ with the same parametrization of Eq. 6. Figure 9 shows the cocktail of electrons from different photonic sources in Au+Au collisions at $\sqrt{s_{NN}} = 62.4$ GeV for MB events. The electrons from photon conversions and from π^0 Dalitz decays are the largest contributions to the total cocktail background. The invariant yields of the candidate electrons are shown as black filled circles. There is more background from photon conversions in this measurement than in [9]. This is the result of the removal of the helium bag and the installation of the HBD in the 2010 data taking, which increases the rate of photon conversions before the tracking detectors. Most of the conversions that are removed using the cocktail are produced before the HBD, i.e. the beampipe, entrance window and gas. Only a very small portion (3%) of the conversions subtracted using the cocktail come from the HBD itself.

The contribution from direct photons is significant for $p_T > 3$ GeV/c. For the contribution from direct photons, we use the measured p_T spectra from ISR R806, R807, R810 experiments [36] and $N_{\rm coll}$ scaling for each centrality bin. The electron spectra from K_{e3} decays at

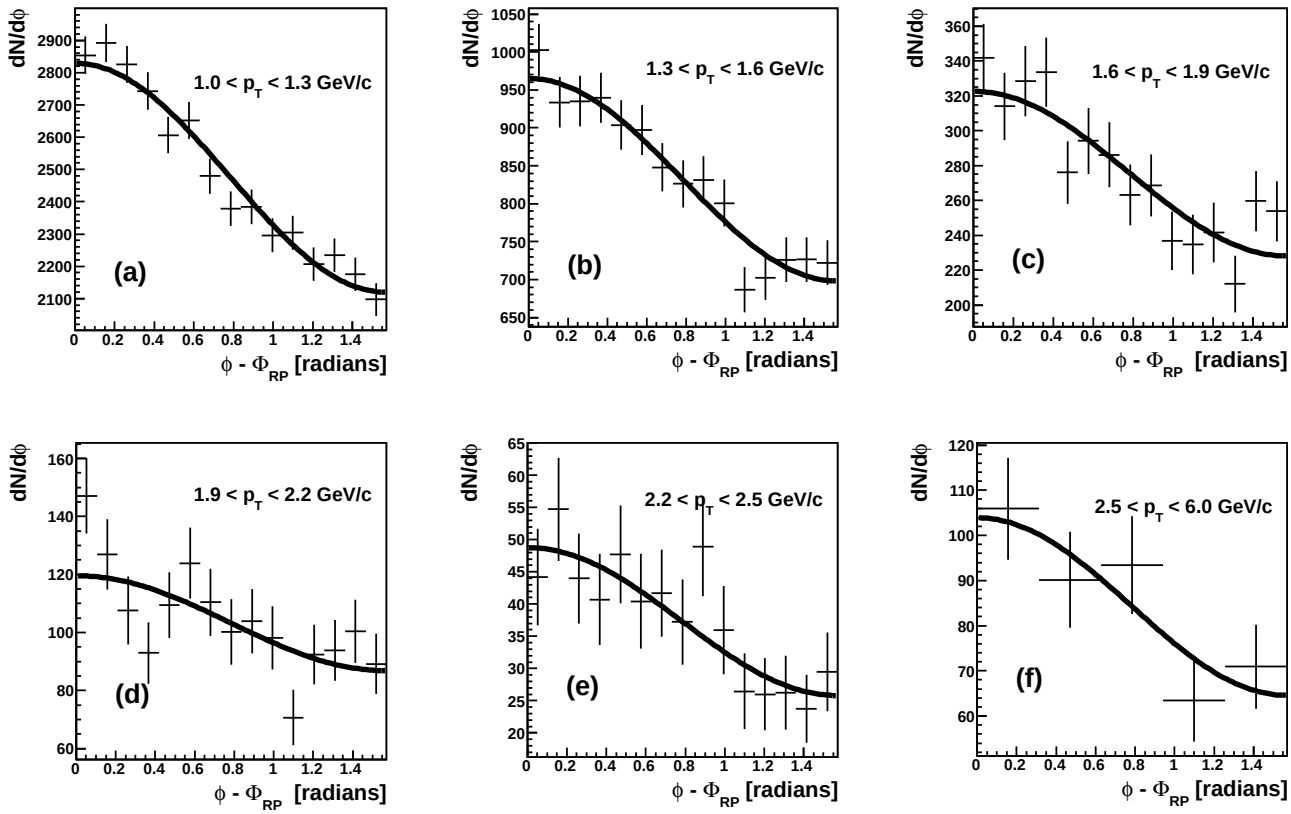

FIG. 7. Candidate electron yield with respect to the RP for different p_T bins for events with centrality 20%–40% and fitted with the function $\frac{dN}{d\phi} = N_0(1 + 2v_2 \cos 2(\phi - \Phi_{\rm RP}))$. The p_T bins are as indicated.

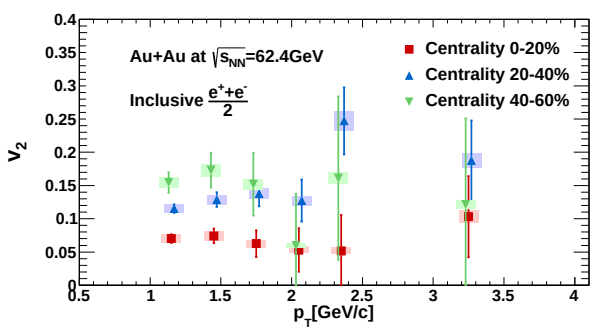

FIG. 8. (Color online) Candidate electron v_2 as a function of p_T in Au+Au collisions at $\sqrt{s_{NN}}$ =62.4 GeV for three different centrality bins. The systematic uncertainty is shown as boxes.

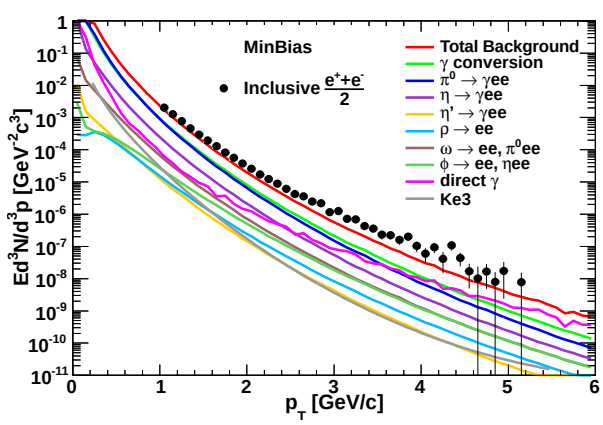

FIG. 9. (Color online) Invariant yield of (black dots) candidate electrons and (solid lines) electrons calculated from different photonic sources in Au+Au collisions at $\sqrt{s_{NN}}$ =62.4 GeV for MB events.

$\sqrt{s_{NN}} = 62.4$ GeV are obtained by a full GEANT simulation of the PHENIX detector and the detector tracking algorithm. Because of a limited amount of experimental data on the J/ψ p_T spectrum at midrapidity in Au+Au collisions at this energy, electrons from J/ψ decays are not subtracted. However, this background is small compared to the dominant backgrounds from pion decays and photon conversions.

The v_2 of photonic electrons is calculated using a cocktail of sources. The PHENIX measurement of v_2 of charged π in Au+Au collisions at $\sqrt{s_{NN}} = 62.4$ GeV [18]

is used to estimate the parent π^0 v_2 distribution. It is known that the measurements of the v_2 of pions and kaons are the same as function of transverse kinetic energy [37],where transverse kinetic energy is $KE_T = \sqrt{p_T^2 + m_o^2} - m_0$. Hence we assume that the v_2 of other mesons in the cocktail have the same v_2 values as a function of transverse kinetic energy as neutral pions. We assume the parent v_2 is negligible for electrons from K_{e3} decays and direct photons. The first background source is small for $p_T < 3.5$ GeV/c where we report v_2 data. To account for possible flow of direct photons we increased the total systematic uncertainty of photonic v_2 as described in the next subsection.

Figure 10 shows the estimated v_2 of photonic electrons as a function of p_T for different centrality bins.

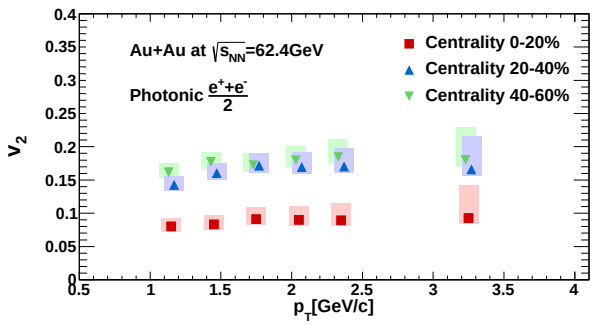

FIG. 10. (Color online) v_2 of photonic electrons calculated as the sum of different photonic sources in Au+Au collisions at $\sqrt{s_{NN}} = 62.4$ GeV for three different centrality bins. Shaded boxes show the systematic uncertainties.

E. Systematic Uncertainties

Systematic uncertainties in the candidate electron measurement include an overall 4% contribution because of the acceptance. This was evaluated by calculating the difference in the geometrical matching between the simulation and the real data. Other systematic uncertainties depend on p_T and are correlated. For example, different choices in eID cuts, loose and tight, were used to evaluate the systematic uncertainties due to eID cuts. The variation between these sets is approximately independent of p_T at a level of 7%. Alternative choices of HBD swapping normalization contribute 0.5% to the systematic uncertainty, while different methods of selecting on HBD charge produced a p_T-dependent systematic uncertainty. The alternate cuts include changing the lower threshold of the *hbdq* cut from 10 to 7 p.e., changing the upper cut from 35 p.e. to 30 or 40 p.e. These changes contribute a systematic uncertainty of 10% for $p_T^e < 1.5$ GeV/c and a systematic uncertainty of 5% for $1.5 < p_T^e < 6$ GeV/c.

Uncertainties in the cocktail method are mainly from the p_T-dependent uncertainties in the parent π^0 spectra which are taken from published data of Au+Au collisions at $\sqrt{s_{NN}} = 62.4$ GeV [19]. The uncertainties from the ratio of light mesons to pion yields are also extracted from published data [33–35].

We also assign a systematic uncertainty of 10% for the amount of material in the GEANT simulation used for the detector in the estimation of electrons from photon conversions, a systematic uncertainty of 20% from the fits of direct photons and a conservative systematic uncertainty of 50% for the electrons from K_{e3} decays.

All these uncertainties are listed in Table II and are propagated into the uncertainties of the heavy-flavor electron spectra by adding them in quadrature.

TABLE II. Systematic uncertainties in the yield of heavy-flavor electrons

Source	Description
acceptance	4%
central arm eID cuts	7%
HBD swapping	0.5%
HBD charge cut	p_T dependent, 5% to 10%
cocktail	p_T dependent, 10% to 15%
photon conversions (in GEANT material)	10%
direct photon yield,	20%
K_{e3}	0.25%

The systematic uncertainties on the v_2 measurement include the uncertainty in electron candidate v_2 and the uncertainty in the photonic electron v_2. The uncertainty in electron candidate v_2 is because of the RP resolution

TABLE III. Summary of fit characteristics for the invariant cross section of heavy-flavor electrons in p+p collisions at $\sqrt{s_{NN}} = 62.4$ GeV [38–40], as shown in Fig. 13

p_T (GeV/c)	Fit Value (cm^{2}GeV$^{-2}c^3$)	Relative Uncertainty
1.1	4.82×10^{-32}	0.061
1.3	1.88×10^{-32}	0.038
1.5	7.89×10^{-33}	0.038
1.7	3.55×10^{-33}	0.045
1.9	1.69×10^{-33}	0.049
2.1	8.44×10^{-34}	0.052
2.3	4.40×10^{-34}	0.055
2.5	2.39×10^{-34}	0.061
2.7	1.34×10^{-34}	0.070
2.9	7.74×10^{-35}	0.083
3.1	4.60×10^{-35}	0.10
3.4	2.21×10^{-35}	0.13
3.8	8.92×10^{-36}	0.17
4.2	3.87×10^{-36}	0.219
4.6	1.79×10^{-36}	0.27
5.0	8.72×10^{-37}	0.32

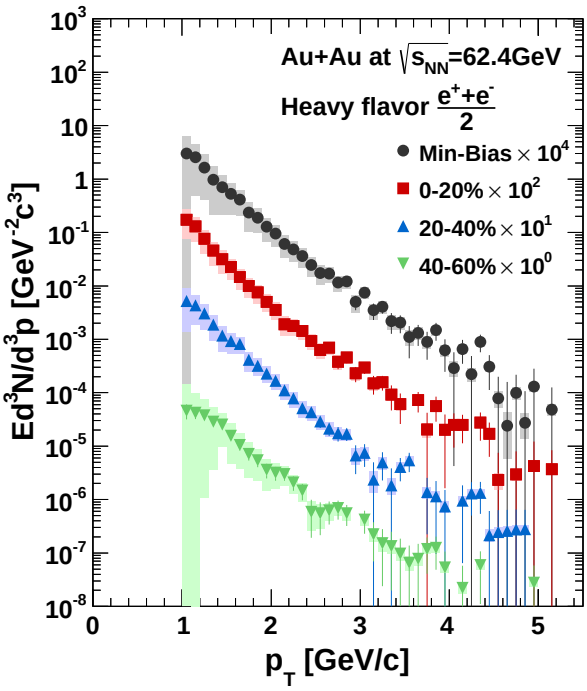

FIG. 11. (Color online) Invariant yield of heavy-flavor electrons measured in Au+Au collisions at $\sqrt{s_{NN}} = 62.4$ GeV for different centrality bins. The yields are scaled by powers of 10 for clarity. The uncertainty bars (boxes) show the statistical (systematic) uncertainties.

(5%). The systematic uncertainty is 8% for central v_2 and 5% for midcentral photonic electrons. We find a systematic uncertainty of 4% due to the uncertainties of the relative ratio of different photonic-electron sources to the photonic electron v_2.

We also assign an additional systematic uncertainty because of possible flow of direct photons as observed in Au+Au collisions at $\sqrt{s_{NN}}$ =200 GeV [41], which was assumed to be zero in our calculation of photonic flow. This additional systematic uncertainty was calculated assuming that direct photon flow is the same as that of π^0.

IV. RESULTS AND DISCUSSION

A. Heavy Flavor Electron Yield

To extract the invariant yield of heavy-flavor electrons, the photonic electron background is subtracted from the invariant yield of candidate electrons for each centrality bin.

$$E\frac{d^3N_{\rm heavyflavor}}{d^3p} = E\frac{d^3N_{\rm inclusive}}{d^3p} - E\frac{d^3N_{\rm cocktail}}{d^3p}, \quad (7)$$

i.e. the data shown in Fig 6 minus the centrality-dependent cocktail comparable to Fig 9. Figure 11 shows the invariant yield of heavy flavor electrons as a function of p_T in four different centrality ranges, MB, 0 to 20%, 20%–40%, and 40%–60%. The error bars and error boxes represent respectively the statistical and systematic uncertainties in the heavy-flavor electron measurement.

Figure 12 shows the signal to background ratio S/B (Eq. 8), in MB events and for the three centrality classes used in this analysis.

$$S/B = \frac{N_{\rm hf}}{N_{\rm photonic}}, \quad (8)$$

where $N_{\rm hf}$ is the yield of heavy-flavor electrons, $N_{photonic}$ is the yield of photonic electrons, i.e. the data shown in Fig 6 divided by the centrality-dependent cocktail comparable to Fig 9. S/B increases with p_T. At low p_T the candidate electrons are primarily from the photonic sources. At high p_T, electrons from heavy flavor meson decays start to dominate the candidate electron yield.

As a baseline, there are three available p+p results from the ISR [38–40] that are shown in Fig. 13. Table III shows the value of the fit and its relative uncertainty for each p_T point used to calculate R_{AA}. These data sets are simultaneously fit to a power-law function:

$$yield = \frac{a}{(p_T + b)^n}, \quad (9)$$

where the parameters are determined to be $a = 1.21 \pm 3.55 \times 10^{-28}$, $b = 1.015 \pm 0.39$ GeV/c, and $n = 10.45 \pm 1.43$, as shown in Fig. 13.

To compare the Au+Au data with p+p results, we divide the Au+Au data by the number of binary collisions, $N_{\rm coll}$. For each of the three centrality classes, Table I lists the $N_{\rm coll}$ values. Figure 14 compares the invariant yield of the heavy-flavor electrons per binary collision in 0%–20%, 20%–40%, 40%–60% centrality bins and MB data in Au+Au collisions at $\sqrt{s_{NN}} = 62.4$ GeV. The invariant cross section of heavy-flavor electrons in p+p collisions at $\sqrt{s_{NN}} = 62.4$ GeV is derived from the highest statistics heavy-flavor electron measurement [38] that was performed at the ISR. These results are scaled by the inelastic cross section at $\sqrt{s_{NN}} = 62.4$ GeV, $\sigma_{pp} = 35.9$ mb [42], and plotted in Fig. 14(e).

The fixed-order-plus-next-to-leading-log (FONLL) prediction [43] (red curve) is also shown in Fig. 14. In Au+Au collisions at $\sqrt{s_{NN}} = 62.4$ GeV, the yield of heavy-flavor electrons per binary collision is higher than the ISR results in p+p collisions, while the ISR p+p results are consistent with the upper limit of the FONLL prediction.

To further study the modification of the yield of heavy-flavor electrons in Au+Au collisions at $\sqrt{s_{NN}} = 62.4$ GeV, the invariant yield per binary collision $N_{\rm coll}$ of heavy-flavor electrons is integrated across three p_T bins as shown in Fig. 15. At $N_{\rm coll} = 1$ the p+p points come from the three published ISR measurements [38–40].

At low p_T ($1.5 < p_T < 2.5$ GeV/c), an enhancement of the heavy flavor electron yield is observed in the 0%–20%

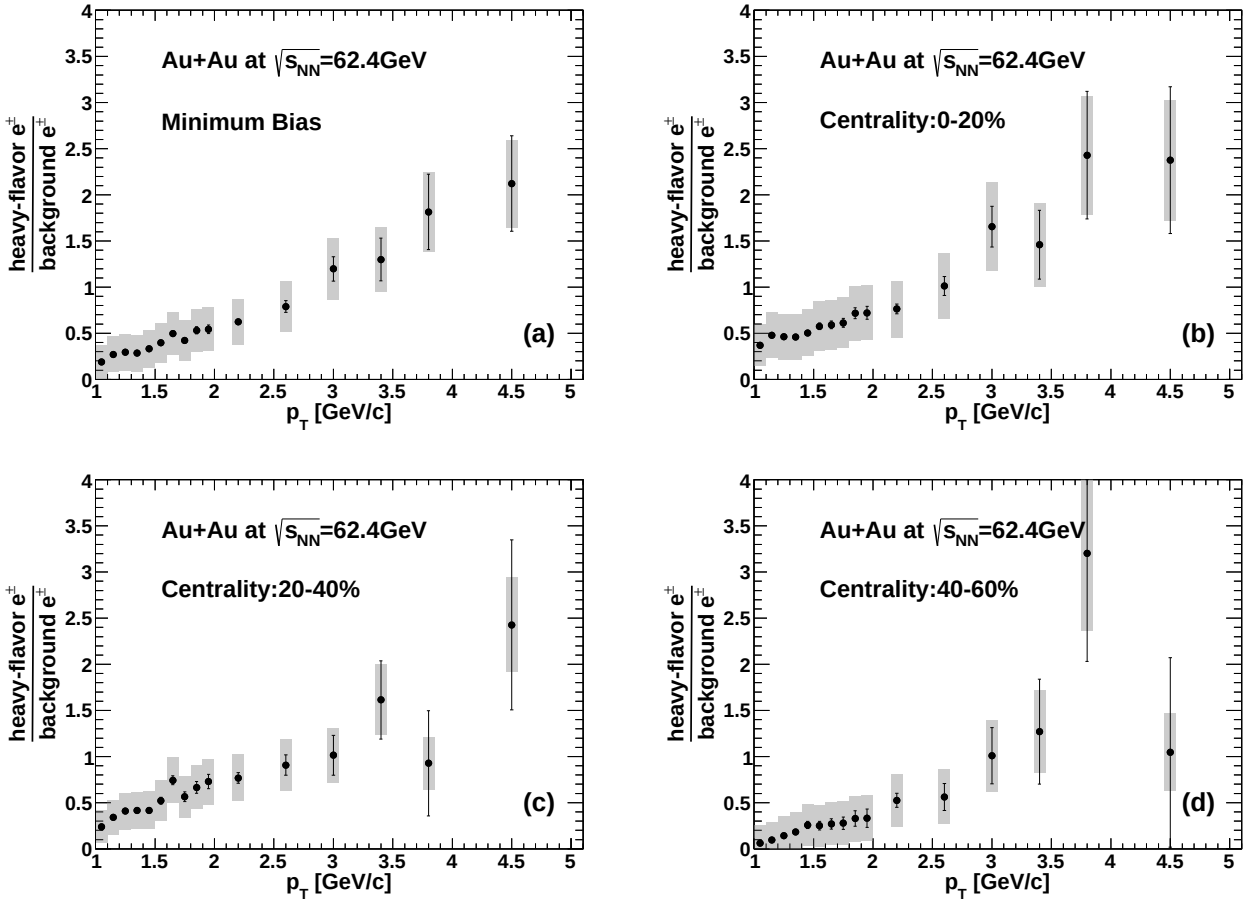

FIG. 12. Ratio of the heavy-flavor electrons (signal) to photonic electrons (background) in Au+Au collisions at $\sqrt{s_{NN}} = 62.4$ GeV for MB events and the three indicated centrality classes that are used in this analysis.

and 20%–40% centrality bins relative to the yield in p+p collisions, while the more peripheral 40%–60% centrality bin is consistent with the p+p yield, within uncertainties. In the higher p_T ranges, $2.5 < p_T < 3.5$ GeV/c and $3 < p_T < 5$ GeV/c, enhancement is observed relative to p+p in all centrality bins. A scenario with only heavy quark energy loss in a deconfined medium would show a pattern of increasing suppression with collision centrality, contrary to what is observed here. This suggests that other mechanisms are present.

We also calculate the nuclear-modification factor R_{AA}, which is the ratio of the yield per binary collision in Au+Au reactions divided by the yield in p+p collisions. The R_{AA} vs p_T are shown in Fig. 16 for 3 different centrality classes and for MB. The yield in p+p collisions is taken from the combined fit to the three ISR data sets [38–40]. The statistical uncertainty on R_{AA} is taken from the statistical uncertainty on the heavy-flavor electron yield measured in Au+Au collisions shown in Fig 11. The systematic uncertainty on R_{AA} is a quadrature sum of the systematic uncertainty on the heavy flavor electron yield in Au+Au collisions and the statistical uncertainty on the fit used to represent the denominator. At low p_T, where the fit to the p+p denominator is relatively well constrained, the systematic uncertainty on R_{AA} is dominated by the systematic uncertainty on the measured heavy-flavor electron yield in Au+Au. At high p_T, where the S/B ratio for heavy-flavor electrons in Au+Au collisions is relatively high and the fit representing the p+p denominator is not well constrained, the systematic uncertainty on R_{AA} is dominated by the uncertainty propagated from the fit parameters. The R_{AA} is consistently larger than unity with the exception of low-p_T data in peripheral collisions. In contrast to the heavy-flavor results, the π^0 data at 62 GeV show a suppression that increases with centrality [19].

These R_{AA} values for electrons from heavy-flavor decay in Au+Au collisions at 62.4 GeV are compared to other R_{AA} results from d+Au, Cu+Cu, and Au+Au collisions at $\sqrt{s_{NN}} = 200$ GeV (data from [9, 21]), as shown in Fig. 17. At 200 GeV the heavy-flavor R_{AA} first increases with centrality then decreases, consistent with a competition between two mechanisms. At 62.4 GeV the competition, if present, favors heavy-flavor enhancement over suppression. This is consistent with previous results with hadrons where the Cronin enhancement in-

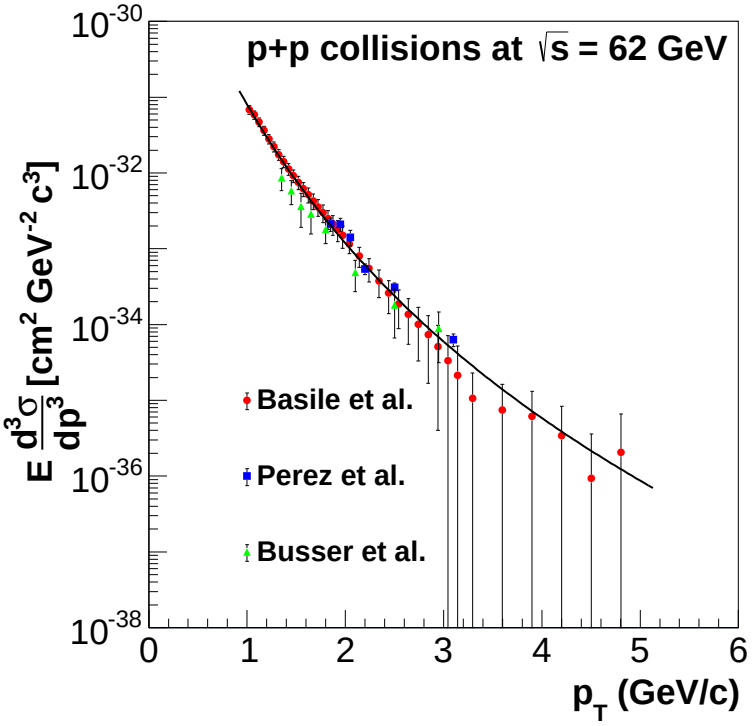

FIG. 13. (Color online) Invariant cross section of heavy-flavor electrons in p+p collisions at $\sqrt{s_{NN}} = 62.4$ GeV [38–40]. The curve is a combined power-law fit (see Table III.

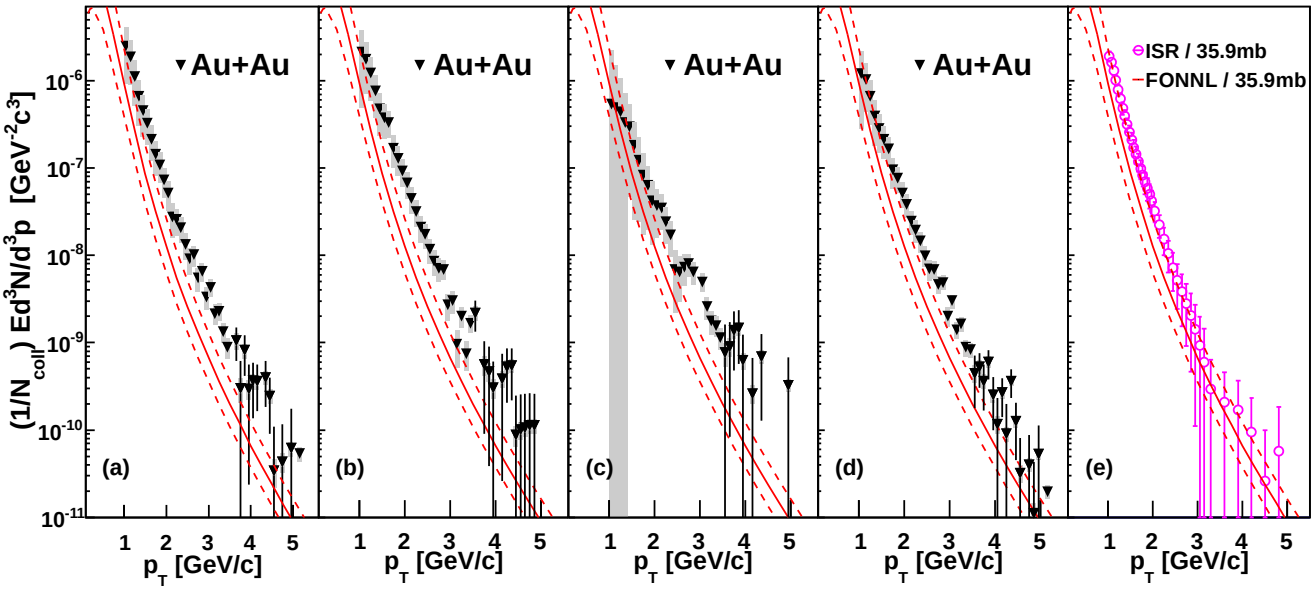

FIG. 14. (Color online) Invariant yield of heavy-flavor electrons per binary collisions in Au+Au collisions at $\sqrt{s_{NN}} = 62.4$ GeV for (a) MB, (b) 0%–20%, (c) 20%–40%, (d) 40%–60%, and (e) p+p collisions at $\sqrt{s_{NN}} = 62.4$ GeV measured in ISR experiments. The curves are (red solid) FONLL calculations and (red dash) upper and lower limits.

creases as the collision energy decreases [44]. This competition between Cronin enhancement, flow, and suppression produces a different pattern for R_{AA} for light mesons (Fig. 18).

To estimate how rapidly the Cronin effect on heavy-flavor production could change from $\sqrt{s_{NN}} = 200$ GeV to 62 GeV, we have performed PYTHIA calculations with different numerical k_T parameters to estimate the possible size of the enhancement due to an increase in initial-state multiple scattering. Increasing k_T from 0 to 1.5 GeV/c enhances the yield of electrons from charm decay by a factor of 2.5 for $2 < p_T < 3$ GeV/c. At 200 GeV this en-

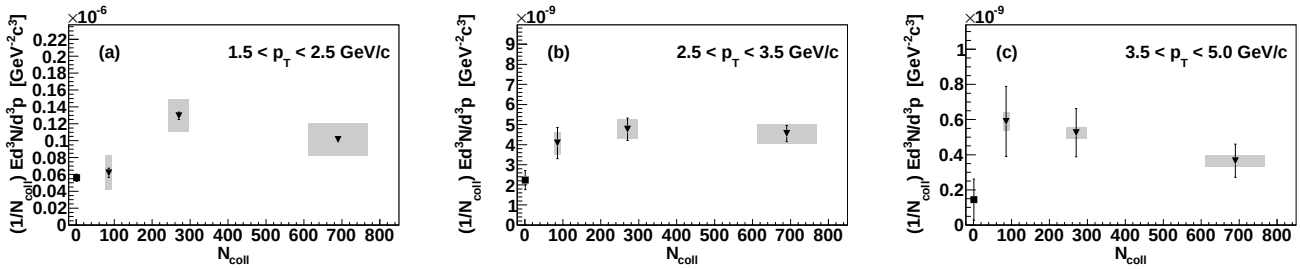

FIG. 15. Integrated invariant yield per binary collision vs $N_{\rm coll}$ for heavy-flavor electrons in Au+Au collisions at $\sqrt{s_{NN}}$ = 62.4 GeV for the indicated $p_T{}^e$ ranges. The data point at $N_{\rm coll}$ =1 is for p+p collisions.

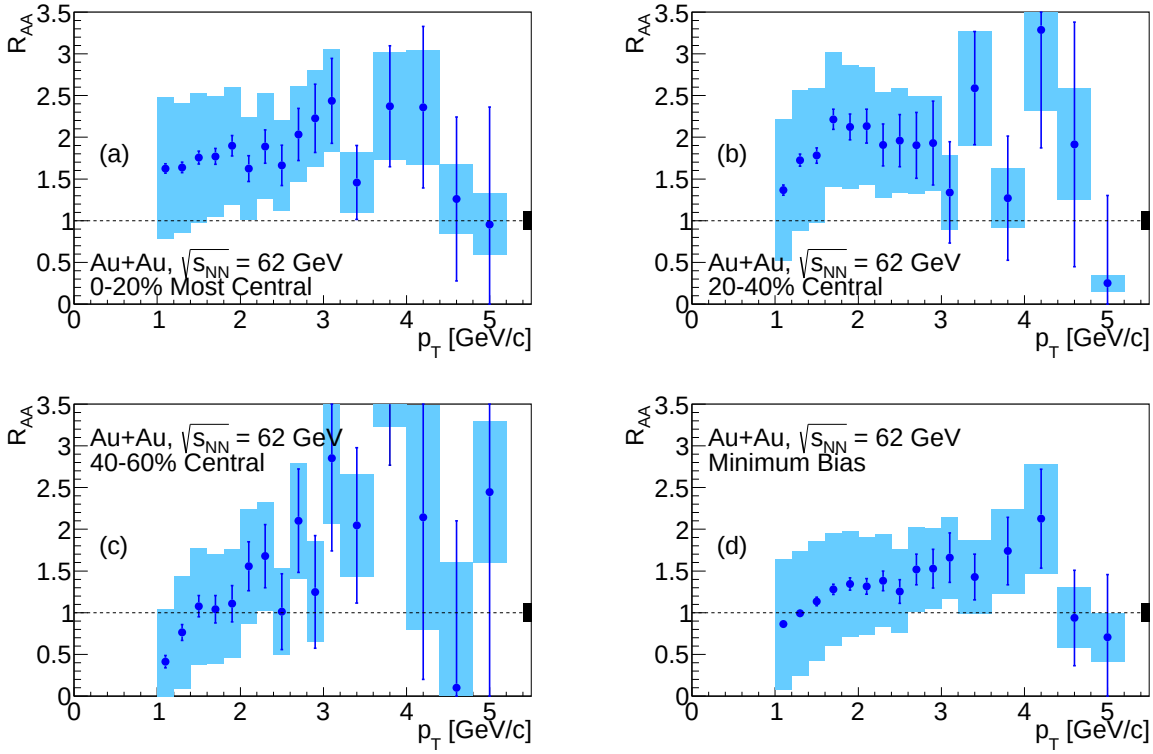

FIG. 16. (Color online) The R_{AA} for electrons from heavy-flavor decays in Au+Au collisions at $\sqrt{s_{NN}}$ = 62.4 GeV for the indicated centralities. The error bars (boxes) represent the statistical (systematic) uncertainties. The global uncertainty due to the uncertainty in $N_{\rm coll}$ for each centrality is given by the box on the right side of each plot.

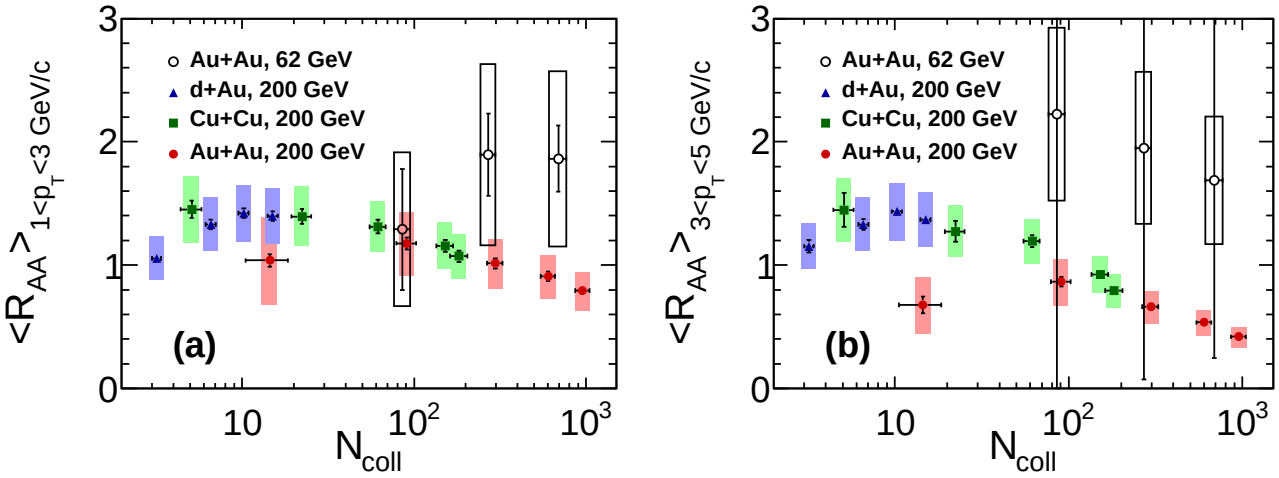

FIG. 17. (Color online) The R_{AA} values for electrons from heavy-flavor decay in Au+Au collisions at 62.4 GeV with the R_{AA} results from d+Au, Cu+Cu, and Au+Au collisions at $\sqrt{s_{NN}}$ = 200 GeV (data from [9, 21]). The error bars (boxes) represent the statistical (systematic) uncertainties. The p_T ranges are as indicated: (a) $1 < p_T < 3$ GeV/c and (b) $3 < p_T < 5$ GeV/c.

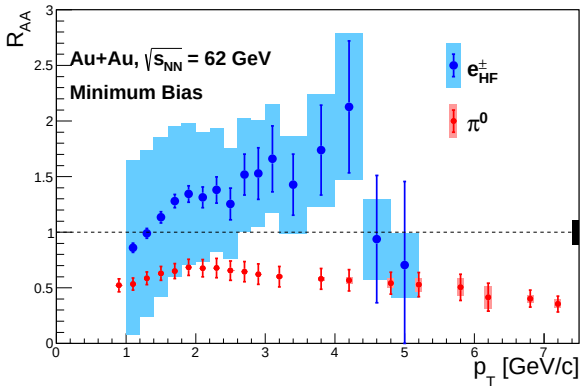

FIG. 18. (Color online) The R_{AA} values from heavy-flavor decay for electrons and π^0 [19] in Au+Au collisions at 62.4 GeV. The error bars (boxes) show the statistical (systematic) uncertainties.

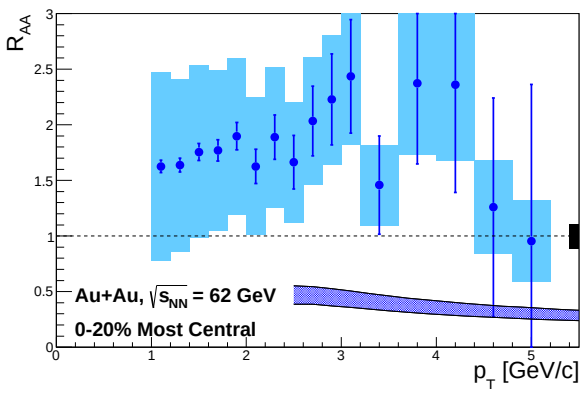

FIG. 19. (Color online) The nuclear modification factor R_{AA} for electrons from heavy-flavor decays in 0%–20% central Au+Au collisions at $\sqrt{s_{NN}} = 62.4$ GeV compared to predictions (dark-blue band) from Vitev *et al.* [13, 45].

hancement is only a factor of 1.5. The observed enhancement of heavy flavor electrons could be due to less energy loss in the medium at 62.4 GeV, a larger Cronin enhancement in the initial state at 62.4 GeV, or a combination of these factors. In addition to the Cronin enhancement, gluon anti-shadowing may increase the charm cross section in Au+Au collision at 62.4 GeV, and cause the overall enhancement of the heavy-flavor electron yield per $N_{\rm coll}$ compared to scaled p+p collisions.

Vitev has predicted R_{AA} using his model of heavy-flavor energy-loss [13, 45]. Figure 19 shows that these calculations, which include both energy-loss of heavy quarks inside a QGP as well as dissociation of D and B mesons, significantly underpredict the measured data.

As a complementary study of the change of the heavy-flavor electron yield from peripheral to central collisions,

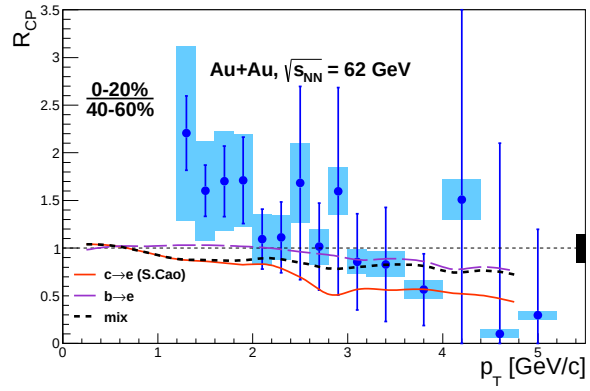

FIG. 20. (Color online) Heavy-flavor electron R_{CP} between centrality 0%–20% and 40%–60% in Au+Au collisions at $\sqrt{s_{NN}} = 62.4$ GeV. The curves are calculated using a model based on energy loss [46, 47].

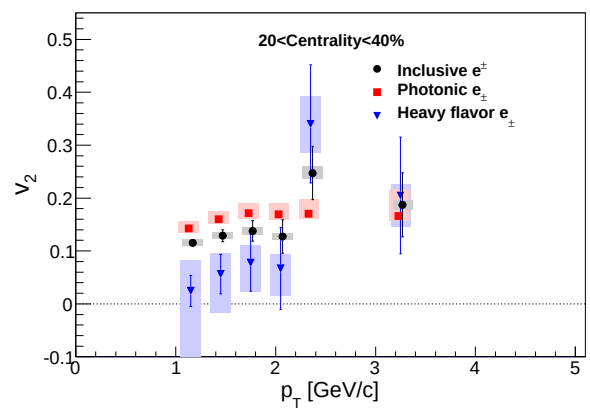

FIG. 21. (Color online) Candidate (inclusive), photonic, and heavy-flavor electron v_2 in Au+Au collisions at $\sqrt{s_{NN}} = 62.4$ GeV for 20%–40% centrality.

we measure R_{CP} as defined by:

$$R_{CP} = \frac{\left\langle N_{\rm coll}^{\rm peripheral} \right\rangle \times dN^{e}_{\rm AuAu,central}/dp_T}{\left\langle N_{\rm coll}^{\rm central} \right\rangle \times dN^{e}_{\rm AuAu,peripheral}/dp_T}. \quad (10)$$

The yield from the 0%–20% centrality bin and 40%–60% centrality bin are used for the numerator and denominator of R_{CP} respectively. Fig. 20 shows R_{CP} is above 1 for p_T below 1 GeV/c and is consistent with 1 at higher transverse momenta. The curves in Fig. 20 are calculated using a model based on energy loss [46, 47].

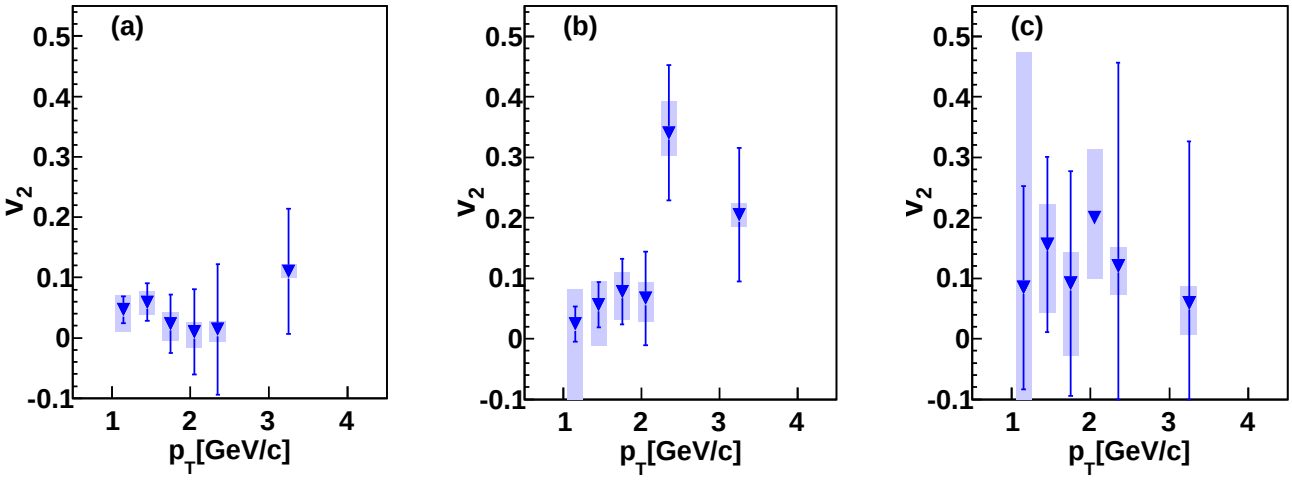

FIG. 22. (Color online) Heavy-flavor electron v_2 in Au+Au collisions at $\sqrt{s_{NN}} = 62.4$ GeV for (a) 0%–20%, (b) 20%–40%, and (c) 40%–60% centrality bins.

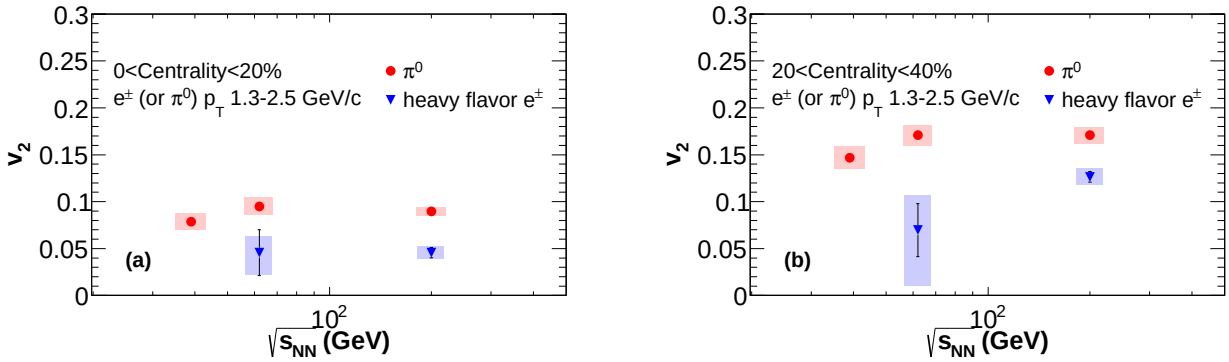

FIG. 23. (Color online) The v_2 of heavy-flavor electrons and π^0 in Au+Au collisions as a function of collision energy in the indicated p_T range of $1.3 < p_T < 2.5$ GeV/c for (a) 0%–20% and (b) 20%–40% centrality.

B. Heavy Flavor Electron v_2

Heavy-flavor-electron v_2 is calculated from candidate-electron v_2, photonic-electron v_2, and S/B as:

$$v_2^{\rm hf} = v_2^{inc}(1 + \frac{1}{S/B}) - v_2^{pho}\frac{1}{S/B}. \qquad (11)$$

Figure 21 shows the measured v_2 results for candidate electrons, photonic and heavy-flavor electrons in the 20%–40% centrality bin to illustrate their relative magnitude. Figure 22 shows the v_2 of heavy-flavor electrons in Au+Au collisions at $\sqrt{s_{NN}} = 62.4$ GeV in 0%–20%, 20%–40% and 40%–60% centrality bins. In the 20%–40% centrality bin, a nonzero v_2 of heavy-flavor electrons is observed for $p_T > 1.5$ GeV/c, which may indicate that charm quarks in the p_T range of this analysis experience some degree of collective motion along with the bulk medium.

To gain further insight into the possible differences in coupling to the medium due to quark mass, the v_2 of heavy-flavor electrons and π^0 for $1.3 < p_T < 2.5$ GeV/c in Au+Au collisions as a function of collision energy are compared in Fig. 23, for 0%–20% centrality and 20%–40% centrality. The plots show that both heavy-flavor electrons and π^0 experience anisotropic flow in Au+Au collisions at $\sqrt{s_{NN}} = 62.4$ GeV and 200 GeV. The v_2 for heavy-flavor electrons is lower than that for π^0. We note that the π^0 is a fully reconstructed meson, while the electrons from heavy-flavor decays are daughter products from the decay of charm and bottom mesons and baryons, and therefore the electron p_T does not necessarily represent the p_T of the parent hadron.

Because the heavy-flavor electrons are decay products from heavy flavor hadrons which may come from recombination of a heavy quark with a light quark from the bulk [47], heavy-flavor hadrons could acquire v_2 as a consequence of recombination. Hence, a nonzero v_2 of heavy flavor electrons does not necessarily imply a nonzero v_2 of

charm quarks. It will be necessary to compare our data with theoretical models with heavy quark flow for further understanding of the collective motion of the heavy quarks in the medium at 62.4 and 200 GeV.

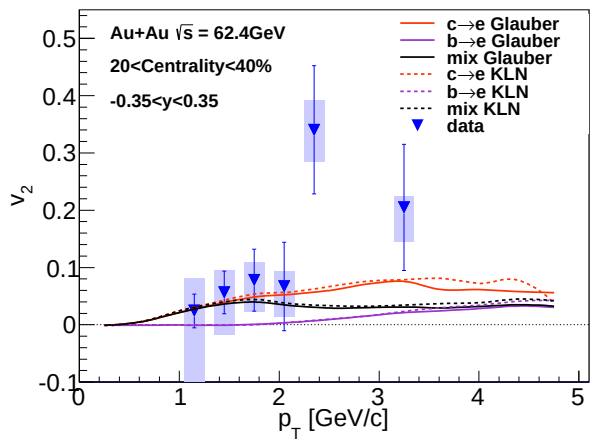

FIG. 24. (Color online) Heavy-flavor electron v_2 in Au+Au collisions at $\sqrt{s_{NN}} = 62.4$ GeV compared with multiple theory curves [46, 48].

Figure 24 shows such a comparison between our v_2 results and theoretical calculations [46, 47], which use the framework of a modified Langevin equation [48] coupled to a (2+1)-dimensional viscous hydrodynamic model [49]. The classical Langevin approach is improved by adding both quasi-elastic scattering and medium-induced gluon radiation for heavy quark energy loss inside the QGP medium. Before the Langevin evolution, heavy quarks are initialized with a leading order perturbative quantum chromodynamics calculation [50] coupled to the nuclear parton distribution function provided in [51]. After traversing the QGP, the heavy quarks hadronize into heavy mesons according to a hybrid model of instantaneous coalescence [52] and PYTHIA 6.4 [53] fragmentation. One set of initial conditions for the hydrodynamic model is used here, MC-Glauber [54]. The calculations are in good agreement with the experimental data up to $p_T = 2$ GeV/c.

Two initial conditions for the hydrodynamic model, MC-Glauber [54] and KLN-CGC [55] are compared in Fig. 24 and the corresponding impact on the final state heavy flavor spectra is displayed. The v_2 predictions in the model show nonzero flow for electrons from heavy-flavor hadrons (Fig. 24), which are mainly D mesons for p_T <5 GeV/c. This model is consistent with the v_2 data at low p_T, within experimental uncertainties.

V. SUMMARY AND CONCLUSIONS

This article presents the measurements of the invariant yield and elliptic flow of electrons from heavy flavor meson semi-leptonic decays in Au+Au collisions at $\sqrt{s_{NN}} = 62.4$ GeV in PHENIX. The integrated invariant yield per binary collision is slightly larger than the yields from prior p+p measurements. This enhancement is different from the suppression observed in previous PHENIX measurements of heavy-flavor electrons in Au+Au at $\sqrt{s_{NN}} = 200$ GeV, but is comparable to the enhancement observed in d+Au collisions at $\sqrt{s_{NN}} = 200$ GeV. Hence it is possible that the initial state Cronin enhancement becomes the dominant effect at low to moderate p_T for heavy quarks at this lower beam energy compared to energy loss in the medium. The measured v_2 of heavy-flavor electrons is positive when averaged across p_T between 1.3 and 2.5 GeV/c. The heavy-flavor v_2 is smaller than the π^0 v_2, and may be caused by collective motion of charm quarks themselves and/or charmed hadrons accruing collective motion through recombination with flowing light partons. Further understanding of the properties of the medium and energy loss of the heavy quarks at 62.4 GeV requires the measurement of cold nuclear matter effects on heavy flavor through p+p or d+A collisions at 62.4 GeV, as well as a separation of the individual contributions from charm and bottom hadrons.

ACKNOWLEDGMENTS

We thank the staff of the Collider-Accelerator and Physics Departments at Brookhaven National Laboratory and the staff of the other PHENIX participating institutions for their vital contributions. We acknowledge support from the Office of Nuclear Physics in the Office of Science of the Department of Energy, the National Science Foundation, Abilene Christian University Research Council, Research Foundation of SUNY, and Dean of the College of Arts and Sciences, Vanderbilt University (U.S.A), Ministry of Education, Culture, Sports, Science, and Technology and the Japan Society for the Promotion of Science (Japan), Conselho Nacional de Desenvolvimento Científico e Tecnológico and Fundação de Amparo à Pesquisa do Estado de São Paulo (Brazil), Natural Science Foundation of China (P. R. China), Croatian Science Foundation and Ministry of Science, Education, and Sports (Croatia), Ministry of Education, Youth and Sports (Czech Republic), Centre National de la Recherche Scientifique, Commissariat à l'Énergie Atomique, and Institut National de Physique Nucléaire et de Physique des Particules (France), Bundesministerium für Bildung und Forschung, Deutscher Akademischer Austausch Dienst, and Alexander von Humboldt Stiftung (Germany), Hungarian National Science Fund, OTKA (Hungary), Department of Atomic Energy and Department of Science and Technology (India), Israel Science Foundation (Israel), National Research Foundation of Korea of the Ministry of Science, ICT, and Future Planning (Korea), Physics Department, Lahore University of Management Sciences (Pakistan), Ministry of Education and Science, Russian Academy of Sciences, Fed-

eral Agency of Atomic Energy (Russia), VR and Wallenberg Foundation (Sweden), the U.S. Civilian Research and Development Foundation for the Independent States of the Former Soviet Union, the Hungarian American Enterprise Scholarship Fund, and the US-Israel Binational Science Foundation.

[1] K. Adcox *et al.* (PHENIX Collaboration), "Formation of dense partonic matter in relativistic nucleus-nucleus collisions at RHIC: Experimental evaluation by the PHENIX collaboration," Nucl. Phys. A **757**, 184 (2005).

[2] P. Huovinen, P. F. Kolb, Ulrich W. Heinz, P. V. Ruuskanen, and S. A. Voloshin, "Radial and elliptic flow at RHIC: Further predictions," Phys. Lett. B **503**, 58 (2001).

[3] S. S. Adler *et al.* (PHENIX Collaboration), "Elliptic flow of identified hadrons in Au+Au collisions at $\sqrt{s_{NN}}$=200 GeV," Phys. Rev. Lett. **91**, 182301 (2003).

[4] John Adams *et al.* (STAR Collaboration), "Particle type dependence of azimuthal anisotropy and nuclear modification of particle production in Au+Au collisions at $\sqrt{s_{NN}}$=200 GeV," Phys. Rev. Lett. **92**, 052302 (2004).

[5] K. Adcox *et al.* (PHENIX Collaboration), "Suppression of hadrons with large transverse momentum in central Au+Au collisions at $\sqrt{s_{NN}}$=130 GeV," Phys. Rev. Lett. **88**, 022301 (2002).

[6] S. S. Adler *et al.* (PHENIX Collaboration), "Suppressed π^0 production at large transverse momentum in central Au+Au collisions at $\sqrt{s_{NN}}$=200 GeV," Phys. Rev. Lett. **91**, 072301 (2003).

[7] J. Adams *et al.* (STAR Collaboration), "Transverse momentum and collision energy dependence of high p_T hadron suppression in Au+Au collisions at ultrarelativistic energies," Phys. Rev. Lett. **91**, 172302 (2003).

[8] A. Adare *et al.* (PHENIX Collaboration), "Energy loss and flow of heavy quarks in Au+Au collisions at $\sqrt{s_{NN}}$=200 GeV," Phys. Rev. Lett. **98**, 172301 (2007).

[9] A. Adare *et al.* (PHENIX Collaboration), "Heavy-quark production in $p+p$ and energy loss and flow of heavy quarks in Au+Au collisions at $\sqrt{s_{NN}}$=200 GeV," Phys. Rev. C **84**, 044905 (2011).

[10] B. Abelev *et al.* (ALICE Collaboration), "D meson elliptic flow in non-central Pb-Pb collisions at $\sqrt{s_{NN}}$=2.76 TeV," Phys. Rev. Lett. **111**, 102301 (2013).

[11] Yuri L. Dokshitzer and D. E. Kharzeev, "Heavy quark colorimetry of QCD matter," Phys. Lett. B **519**, 199 (2001).

[12] Nestor Armesto, Andrea Dainese, Carlos A. Salgado, and Urs Achim Wiedemann, "Testing the color charge and mass dependence of parton energy loss with heavy-to-light ratios at RHIC and CERN LHC," Phys. Rev. D **71**, 054027 (2005).

[13] Rishi Sharma, Ivan Vitev, and Ben-Wei Zhang, "Light-cone wave function approach to open heavy flavor dynamics in QCD matter," Phys. Rev. C **80**, 054902 (2009).

[14] Min He, Rainer J. Fries, and Ralf Rapp, "Heavy-quark diffusion and hadronization in quark-gluon plasma," Phys. Rev. C **86**, 014903 (2012).

[15] Jan Uphoff, Oliver Fochler, Zhe Xu, and Carsten Greiner, "Open heavy flavor in Pb+Pb collisions at $\sqrt{s}$=2.76 TeV within a transport model," Phys. Lett. B **717**, 430 (2012).

[16] P. B. Gossiaux and J. Aichelin, "Towards an understanding of the RHIC single-electron data," Phys. Rev. C **78**, 014904 (2008).

[17] L. Adamczyk *et al.* (STAR Collaboration), "Observation of an energy-dependent difference in elliptic flow between particles and antiparticles in relativistic heavy ion collisions," Phys. Rev. Lett. **110**, 142301 (2013).

[18] A. Adare *et al.* (PHENIX Collaboration), "Systematic study of azimuthal anisotropy in Cu+Cu and Au+Au collisions at $\sqrt{s_{NN}}$=62.4 and 200 GeV," (to be published), arXiv:1412.1043.

[19] A. Adare *et al.* (PHENIX Collaboration), "Evolution of suppression in Au+Au collisions from $\sqrt{s_{NN}}$=39 to 200 GeV," Phys. Rev. Lett. **109**, 152301 (2012).

[20] Ivan Vitev, "Jet quenching at intermediate RHIC energies," Phys. Lett. B **606**, 303 (2005).

[21] A. Adare *et al.* (PHENIX Collaboration), "Cold-nuclear-matter effects on heavy-quark production in d+Au collisions at $\sqrt{s_{NN}}$=200 GeV," Phys. Rev. Lett. **109**, 242301 (2012).

[22] P. B. Straub *et al.*, "Nuclear dependence of high-χ_T hadron and high-T hadron-pair production in p-A collisions at $\sqrt{s}$=38.8 GeV," Phys. Rev. Lett. **68**, 452 (1992).

[23] K. Adcox *et al.* (PHENIX Collaboration), "PHENIX detector overview," Nucl. Instrum. Methods Phys. Res., Sect. A **499**, 469 (2003).

[24] M. Allen *et al.* (PHENIX Collaboration), "PHENIX inner detectors," Nucl. Instrum. Methods Phys. Res., Sect. A **499**, 549 (2003).

[25] E. Richardson *et al.* (PHENIX Collaboration), "A Reaction Plane Detector for PHENIX at RHIC," Nucl. Instrum. Methods Phys. Res., Sect. A **636**, 99 (2011).

[26] Z. Fraenkel *et al.* (PHENIX Collaboration), "A Hadron blind detector for the PHENIX experiment at RHIC," Nucl. Instrum. Methods Phys. Res., Sect. A **546**, 466 (2005).

[27] W. Anderson *et al.* (PHENIX Collaboration), "Design, construction, operation and performance of a hadron-blind detector for the PHENIX experiment," Nucl. Instrum. Methods Phys. Res., Sect. A **646**, 35 (2011).

[28] K. Adcox *et al.* (PHENIX Collaboration), "PHENIX central-arm tracking detectors," Nucl. Instrum. Methods Phys. Res., Sect. A **499**, 489 (2003).

[29] M. Aizawa *et al.* (PHENIX Collaboration), "PHENIX central arm particle ID detectors," Nucl. Instr. Methods Phys. Res., Sect. A **499**, 508 (2003).

[30] Y. Akiba, R. Begay, J. Burward-Hoy, R. Chappell, D. Crook, *et al.* (PHENIX Collaboration), "Ring imaging Cherenkov detector of PHENIX experiment at RHIC," Nucl. Instrum. Methods Phys. Res., Sect. A **433**, 143 (1999).

[31] L Aphecetche *et al.* (PHENIX Collaboration), "PHENIX calorimeter," Nucl. Instrum. Methods Phys. Res., Sect. A **499**, 521 (2003).

[32] R. Brun, F. Bruyant, M. Maire, A.C. McPherson, and P. Zanarini, "GEANT3, CERN Program Library Long

Write-up W5013," (1987).
[33] S. S. Adler *et al.* (PHENIX Collaboration), "Common suppression pattern of η and π^0 mesons at high transverse momentum in Au+Au collisions at $\sqrt{s_{NN}}$=200 GeV," Phys. Rev. Lett. **96**, 202301 (2006).
[34] Yu. Riabov (PHENIX Collaboration), "Measurement of leptonic and hadronic decays of ω and ϕ mesons at RHIC by PHENIX," J. Phys. G **34**, S925 (2007).
[35] K Nakamura *et al.* (Particle Data Group), "Reviews of particle physics," J. Phys. G **37**, 075021 (2010).
[36] W. Vogelsang and M. R. Whalley, "A compilation of data on single and double prompt-photon production in hadron-hadron interactions," J. Phys. G **23**, A1 (1997).
[37] A. Adare *et al.* (PHENIX Collaboration), "Deviation from quark number scaling of the anisotropy parameter v_2 of pions, kaons, and protons in Au+Au collisions at $\sqrt{s_{NN}}$=200 GeV," Phys. Rev. C **85**, 064914 (2012).
[38] M. Basile *et al.*, "A measurement of the prompt e production cross-section in proton-proton collisions at $\sqrt{s}$=62.2 GeV," Il Nuovo Cimento A **65**, 421 (1981).
[39] F. W. Busser *et al.*, "A measurement of single electrons, electron pairs, and associated phenomena in proton-proton collisions at the CERN ISR," Nucl. Phys. B **113**, 189 (1976).
[40] P. Perez *et al.*, "Measurement of single electron production up to 45 GeV/c transverse momentum at the CERN ISR," Phys. Lett. B **112**, 260 (1982).
[41] A. Adare *et al.* (PHENIX Collaboration), "Observation of direct-photon collective flow in Au+Au collisions at $\sqrt{s_{NN}}$=200 GeV," Phys. Rev. Lett. **109**, 122302 (2012).
[42] L. Baksay *et al.*, "Measurements of the proton-proton total cross section and small angle elastic scattering at ISR energies," Nucl. Phys. B **141**, 1 (1978).
[43] R. Vogt, (private communication).
[44] S. S. Adler *et al.* (PHENIX Collaboration), "Nuclear effects on hadron production in d+Au and p+p collisions at $\sqrt{s_{NN}}$=200 GeV," Phys. Rev. C **74**, 024904 (2006).
[45] I. Vitev, (private communication).
[46] S. Cao, (private communication).
[47] Shanshan Cao, Guang-You Qin, and Steffen A. Bass, "Heavy quark dynamics and hadronization in ultra-relativistic heavy-ion collisions: collisional versus radiative energy loss," Phys. Rev. C **88**, 044907 (2013).
[48] Shanshan Cao, Guang-You Qin, Steffen A. Bass, and Berndt Mueller, "Collisional vs. radiative energy loss of heavy quark in a hot and dense nuclear matter," Nucl. Phys. A **904-905**, 653c–656c (2013).
[49] Chun Shen and Ulrich Heinz, "Collision energy dependence of viscous hydrodynamic flow in relativistic heavy-ion collisions," Phys. Rev. C **85**, 054902 (2012).
[50] J. F. Owens, "Large-momentum-transfer production of direct photons, jets, and particles," Rev. Mod. Phys. **59**, 465–503 (1987).
[51] Kari J. Eskola, Hannu Paukkunen, and Carlos A. Salgado, "An Improved global analysis of nuclear parton distribution functions including RHIC data," J. High Energy Phys. **07** (2008) 102.
[52] Yongseok Oh, Che Ming Ko, Su Houng Lee, and Shigehiro Yasui, "Heavy baryon/meson ratios in relativistic heavy ion collisions," Phys. Rev. C **79**, 044905 (2009).
[53] Torbjorn Sjostrand, Stephen Mrenna, and Peter Z. Skands, "PYTHIA 6.4 Physics and Manual," J. High Energy Phys. **05** (2006) 026.
[54] Michael L. Miller, Klaus Reygers, Stephen J. Sanders, and Peter Steinberg, "Glauber modeling in high-energy nuclear collisions," Ann. Rev. Nucl. Part. Sci. **57**, 205–243 (2007).
[55] Dmitri Kharzeev, Eugene Levin, and Marzia Nardi, "Color glass condensate at the LHC: Hadron multiplicities in pp, pA and AA collisions," Nucl. Phys. A **747**, 609–629 (2005).